

ESD RECORD COPY

RETURN TO
SCIENTIFIC & TECHNICAL INFORMATION DIVISION
(ESTI) BUILDING 1241

ESD ACCESSION LISTESTI Call No. **AI** **58473**Copy No. **7** of **7** cysESD-TR-67-467
ESTI FILE COPY

3

Solid State Research**1967**

Prepared under Electronic Systems Division Contract AF 19(628)-5167 by

Lincoln Laboratory

MASSACHUSETTS INSTITUTE OF TECHNOLOGY

Lexington, Massachusetts



AD661275

The work reported in this document was performed at Lincoln Laboratory, a center for research operated by Massachusetts Institute of Technology, with the support of the U.S. Air Force under Contract AF 19(628)-5167.

This report may be reproduced to satisfy needs of U.S. Government agencies.

This document has been approved for public release and sale; its distribution is unlimited.

Non-Lincoln Recipients

PLEASE DO NOT RETURN

Permission is given to destroy this document
when it is no longer needed.

3

Solid State Research

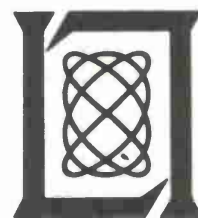
1967

Issued 18 October 1967

Lincoln Laboratory

MASSACHUSETTS INSTITUTE OF TECHNOLOGY

Lexington, Massachusetts



ABSTRACT

This report covers in detail the solid state research work at Lincoln Laboratory for the period 1 May through 31 July 1967. The topics covered are Solid State Device Research, Optical Techniques and Devices, Materials Research, and Physics of Solids.

Accepted for the Air Force
Franklin C. Hudson
Chief, Lincoln Laboratory Office

INTRODUCTION

I. SOLID STATE DEVICE RESEARCH

The variation of detection efficiency with junction depth was determined for two $\text{Pb}_{0.933}\text{Sn}_{0.067}\text{Se}$ photovoltaic detectors. The minority carrier diffusion length was determined from this variation to be 3 and 4μ for the two detectors. Response speeds ranging from less than 5 to 100 nsec were determined for several $\text{Pb}_{1-x}\text{Sn}_x\text{Se}$ detectors. The diode capacitance was typically 2000 pf/mm^2 and the RC time constant ranged between 1 and 5 nsec indicating that the response speed of most detectors is not RC-limited. Photovoltaic response has been observed at temperatures as high as 195°K in several $\text{Pb}_{1-x}\text{Sn}_x\text{Se}$ detectors. The peak response decreased by about a factor of 20 below that determined at 12°K and 77°K .

$\text{Pb}_{1-x}\text{Sn}_x\text{Se}$ diode lasers have been fabricated with output powers as high as 80 mW and external quantum efficiencies of up to 5 percent. The output power of a $\text{Pb}_{0.945}\text{Sn}_{0.055}\text{Se}$ laser at 12°K was found to rise superlinearly, even at the highest power levels, indicating that its internal quantum efficiency has not attained its limiting value and that the output power of this diode is limited by some nonradiative recombination process.

Annealing experiments on $\text{Pb}_{1-x}\text{Sn}_x\text{Te}$ were carried out for the two compositions $x = 0.13$ and $x = 0.17$ at various temperatures and under both metal-saturated and Te-saturated conditions. The solidus lines for the Te-rich and metal-rich side of the phase diagrams have been determined.

Pulsed electron beam pumped lasers prepared from single crystal platelets of CdSe grown in an atmosphere of excess Cd have yielded 300 W of peak output power, an overall power efficiency of 28 percent, and an internal power efficiency of 38 percent at 4.2°K . With increasing temperature, the performance of the lasers fell off more rapidly than was the case in similar high power lasers of CdS. At 77°K , the maximum measured values of peak power, overall efficiency, and internal efficiency were 184 W, 19 percent and 25 percent, respectively. No lasing was observed at temperatures above approximately 100°K .

Epitaxial GaAs with good electrical properties has been grown on GaAs seeds by the $\text{AsCl}_3\text{-Ga-H}_2$ flow system. In order to obtain epitaxial layers which yield high efficiency Gunn effect oscillators, the use of a chelating agent in the preparation of the seed surface was required. Furthermore, large gradations in the impurity concentration of the epitaxial layer occurred whenever growth was initiated before the Ga boat was fully As saturated. This variation is attributed to the effect of As pressure on out-diffusion of the seed dopant into the epitaxial layer. The impurity gradients can be eliminated and high efficiency Gunn effect devices can be obtained by initiating growth only after the Ga boat is saturated.

Gunn effect oscillations as well as current runaway caused by a bulk avalanche of electron-hole pairs in n-type CdTe have been studied. The current runaway occurs after several Gunn oscillations and is accompanied by a drop in voltage below the Gunn threshold and the observation of light-emitting filaments extending from one contact to the other. The experimental results

Introduction

indicate that the avalanche is probably initiated by the traveling high-field Gunn domains. However, the mechanism which sustains the current runaway is not fully understood.

II. OPTICAL TECHNIQUES AND DEVICES

Recent measurements indicate marked improvements in the short-term frequency stability of stable CO₂ lasers. The width of the spurious frequency jitter was typically 6 to 10 kHz for observation times of several seconds, and less than 1 kHz for tens of milliseconds.

Improved efficiency and lifetime have been obtained in sealed-off CO₂ lasers. Continuous heating of the nickel cathode has yielded an operating lifetime greater than 800 hours, without interruption of the discharge.

Detectors of photovoltaic Pb_{1-x}Sn_xSe, operated at 77°K have achieved theoretically optimum operation for kHz and MHz heterodyne frequencies.

A 10.6-μ four-port circulator using free carrier rotation in InSb has been constructed. Isolation ratios of 1000:1 in power have been obtained with insertion losses of 10 percent. The power handling capability is under study.

III. MATERIALS RESEARCH

A simple method has been developed for measuring the concentration of available oxygen (O₂ + H₂O) in inert gases. The rate of increase in resistance of a coiled tungsten filament due to oxidation is measured by measuring the current through the filament at constant voltage.

Single crystals of CrBr₃ about 10 mm on a side have been grown from the vapor in the tapered tip of an evacuated silica ampoule, which is slowly raised out of a vertical resistance furnace heated to 900°C.

Differential thermal analysis has been used to determine the transition temperature between the low- and high-temperature forms of Ag₂Te as a function of hydrostatic pressure up to 14 kbars. X-ray diffraction data for the high-pressure phases Ag₂Te-II and Ag₂Te-III have been indexed on tetragonal cells with $a = 8.92 \text{ \AA}$ and 8.68 \AA , respectively, and $c = 6.09 \text{ \AA}$ in both cases.

The crystal structure of La₄Re₆O₁₉ has been determined by computer analysis of integrated x-ray powder diffraction data. Rhenium-oxygen octahedra share edges and corners to form a three-dimensional network containing sizable voids within which there are La₄O tetrahedra.

Single crystals of RbNiF₃, a transparent ferrimagnetic material which may prove to be useful in Faraday rotation isolators for infrared radiation, have been grown from the melt by the Bridgman method. The absorption coefficient at 10.6 μm, the wavelength of the CO₂ laser, was found to be about 4 cm⁻¹.

Optical and magnetic measurements have shown that CaF₂:U⁺³ crystals usually contain significant amounts of U⁺² and U⁺⁴ ions. The laser threshold has been reduced by a factor of 4 in crystals prepared by a method which decreases the U⁺² and U⁺⁴ concentrations.

An x-ray fluorescence method has been developed for the determination of rhenium and tungsten in $W_{1-x}Re_xO_3$ solid solutions. A method has also been developed for determining iron and yttrium in yttrium-iron garnets (YIG). The total of yttrium and iron is determined by an automatic EDTA titration, and the iron is determined separately by a spectrophotometric method.

IV. PHYSICS OF SOLIDS

The beat frequency observed in the Shubnikov-de Haas data on n-type HgSe is explained by inversion asymmetry splitting of the conduction band when magnetic field induced effects on the electron orbits are taken into account.

Extra transitions seen in electric field modulated magneto-reflection from InSb are attributed mainly to warping of the valence band energy surface and the resulting admixture of close-lying Landau level states.

Magneto-electroreflectivity measurements on the transition from the split-off valence band to conduction band in InAs and InSb at 1.5°K have yielded new values for several band parameters.

The oscillatory magnetorefectivity in bismuth is satisfactorily described by a lineshape calculation which takes into account the nonparabolicity of the energy bands, the k-dependence of the velocity matrix elements, and the anisotropy of the energy surfaces near the L-point. The dependence of the Landau energy levels on the k-vector along the field was derived, with Baraff corrections included.

A reordering of the conduction band with respect to the d-band in nickel is in better agreement with de Haas-van Alphen data and infrared temperature-modulated reflectance data.

Symmetry properties of the cation d-bands for the nonmagnetic corundum structure are shown to place no restriction on whether Ti_2O_3 and V_2O_3 , when structured like corundum, are semiconducting or metallic.

Measurements of the critical point exponents for the paramagnetic susceptibility and the magnetization of $La_{0.5}Sr_{0.5}CoO_3$ give values which are lower than predicted, respectively, by the high-temperature expansion method and the gas-ferromagnet analogy.

Polarization properties and relative intensities of the Raman laser scattering from mixed plasmon-phonon modes in GaAs crystals have been measured and compare favorably with cross-section calculations given in terms of the crystal Raman coefficients which couple the photons to transverse and longitudinal optic modes and to charge density fluctuations.

A reasonable estimate of the quartz Raman susceptibility and cross section has been made from the threshold power and gain for the quartz Raman oscillator pumped by a ruby laser.

The spectral power density of the broad frequency smearing which occurs when a high-power Nd:glass laser beam passes through a CS_2 liquid cell has been studied as a function of input power.

The beam pattern of the 337- μ wavelength oscillation of the far infrared cyanide laser has been mapped out. Also, coherent detection was obtained with a millimeter wave crystal diode detector.

1872

1872

CONTENTS

Abstract	iii
Introduction	v
Organization	xi
Reports by Authors Engaged in Solid State Research	xiii
 I. SOLID STATE DEVICE RESEARCH	 1
A. $Pb_{1-x}Sn_xSe$ Photovoltaic Detectors	1
B. $Pb_{1-x}Sn_xSe$ Diode Lasers	3
C. Isothermal Annealing of $Pb_{1-x}Sn_xTe$	5
D. High Power and Efficiency in CdSe Electron-Beam-Pumped Lasers	6
E. Epitaxial Gallium Arsenide for Gunn Effect Oscillators	7
1. Epitaxial Process	7
2. Electrical Measurements	9
3. Device Problems	9
4. Differential Capacitance Measurements	10
5. Impurity Profiles	10
6. Conclusions	12
F. The Gunn Effect in n-CdTe	12
G. Current Runaway and Avalanche Effects in n-CdTe	15
 II. OPTICAL TECHNIQUES AND DEVICES	 19
A. Stability Measurements of CO_2-N_2-He Lasers at $10.6\mu m$ Wavelength	19
B. Continuous Operation of a Long-Lived Sealed CO_2 Laser Tube. Efficiency of a Sealed CO_2 Laser Tube	21
C. Infrared Heterodyne Detection	23
D. A 10.6-Micron Four-Port Circulator Using Free Carrier Rotation in InSb	23
 III. MATERIALS RESEARCH	 27
A. Measurement of Trace Oxygen and Water Vapor in Inert Gases	27
B. Growth of $CrBr_3$ Single Crystals	30
C. Polymorphism in Ag_2Te at High Pressures and Temperatures	30
D. Characterization and Structure of $La_4Re_6O_{19}$	32
E. Preparation of Transparent Ferrimagnetic Materials	35
F. Properties of Materials for Optically-Pumped Lasers	36
G. Chemical Analysis	36
1. X-ray Fluorescence Analysis of $W_{1-x}Re_xO_3$ Solid Solutions	36
2. Determination of Yttrium and Iron in Yttrium-Iron Garnets	37

Contents

IV. PHYSICS OF SOLIDS	39
A. Electronic Band Structure	39
1. Analysis of Shubnikov-de Haas Results for HgSe	39
2. Warping-Induced Transitions in InSb	40
3. Magneto-Electroreflectance of InAs and InSb at Liquid Helium Temperature	42
4. Magnetoreflexion and the Electronic Energy Bands in Bismuth	42
5. Low Energy Interband Transitions and Band Structure of Nickel	44
6. Symmetry of Cation d-Bands in the Corundum Structure	44
B. Magnetism	46
C. Laser Experiments	47
1. Polarization and Intensity of Raman Scattering From Plasmons and Phonons in Gallium Arsenide	47
2. Stimulated Raman Oscillator	48
3. Frequency Smearing in Nd:Glass Laser Filaments	49
4. Far Infrared Cyanide Laser	51

ORGANIZATION

SOLID STATE DIVISION

A. L. McWhorter, *Head*
P. E. Tannenwald, *Associate Head*
M. J. Hudson, *Assistant*
E. P. Warekois

SOLID STATE THEORY

H. J. Zeiger, *Leader*
M. M. Litvak, *Assistant Leader*

Argyres, P. N.	Landon, S. N.
Chinn, S. R.*	Larsen, D. M.
Dresselhaus, G. F.	Lyons, D. H.†
Hanus, J.	Melanson, G. S., Jr.
Hartung, W. G.	Palm, B. J.‡
Kaplan, T. A.	Sigel, J. L.*
Kelley, P. L.	Stanley, H. E.
Kleiner, W. H.	Van Zandt, L. L.

OPTICS AND INFRARED

R. H. Kingston, *Leader*
R. J. Keyes, *Assistant Leader*

Bates, D. H.	McPhie, J. M.
Bostick, H. A.	Quist, T. M.
Carbone, R. J.	Ross, A. H. M.
Dennis, J. H.	Sullivan, F. M.
Freed, C.	Teich, M. C.
Longaker, P. R.	Zimmerman, M. D.

ELECTRONIC MATERIALS

J. B. Goodenough, *Leader*
A. J. Strauss, *Associate Leader*

Anderson, C. H., Jr.	Lavine, M. C.‡
Andrews, H. I.*	Longo, J. M.
Arnott, R. J.	Mastromattei, E. L.
Banus, M. D.	O'Connor, J. R.
Batson, D. A.	Owens, E. B.
Brebrick, R. F., Jr.	Plonko, M. C.
Button, M. J.	Pollard, E. R.*
Delaney, E. J.	Raccah, P. M.
England, R. E.	Reed, T. B.
Fahey, R. E.	Roddy, J. T.
Ferretti, A.	Searles, I. H.
Finn, M. C.	Sohn, J. B.
Hilsenrath, S.	Soracco, D. J.
Iseler, G. W.	Steininger, J. M.
Kafalas, J. A.	Wheatley, G. E.
LaFleur, W. J.	

SOLID STATE PHYSICS

J. G. Mavroides, *Leader*
G. B. Wright, *Assistant Leader*

Burke, J. W.	Melngailis, J.
Carman, R. L.	Menyuk, N.
Dickey, D. H.	Murphy, H. C.
Dresselhaus, M. S.	Nicoli, D. F.†
Dwight, K., Jr.	Nill, K. W.
Feinleib, J.	Parker, C. D.
Feldman, B.	Perry, F. H.
Fulton, M. J.	Scouler, W. J.
Groves, S. H.	Stickler, J. J.*
Johnson, E. J.	Strahm, N. D.*
Kernan, W. C.	Thaxter, J. B.
Kolesar, D. F.	Tichovolsky, E. J.*
Krag, W. E.	Weber, R.

APPLIED PHYSICS

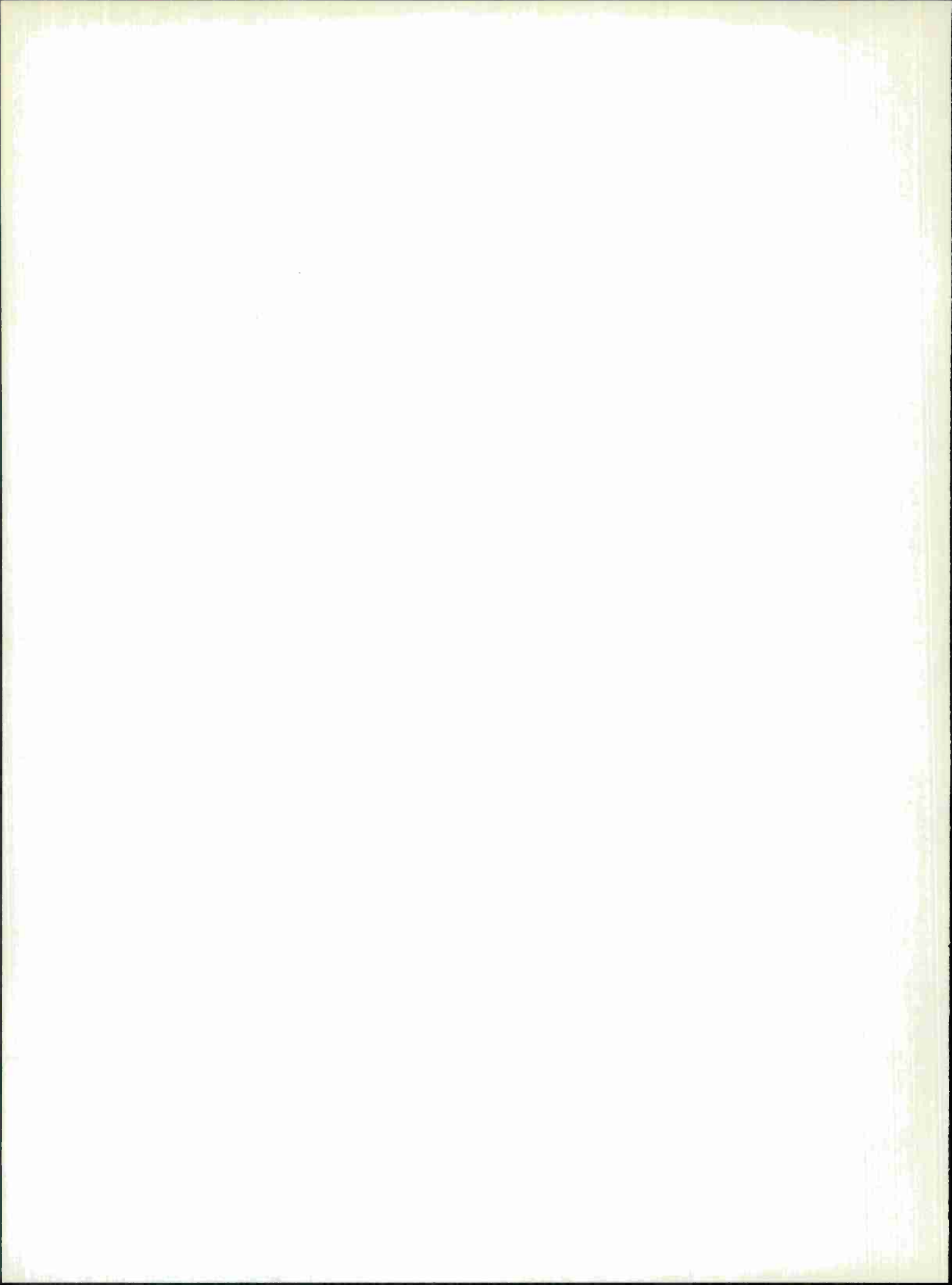
J. O. Dimmock, *Leader*
T. C. Harman, *Assistant Leader*
I. Melngailis, *Assistant Leader*

Butler, J. F.	Donnelly, J. P.	Matthews, W.*	Paladino, A. E.
Calawa, A. R.	Finne, P. C.	Mooradian, A.	Phelan, R. J., Jr.
Carter, F. B.	Foyt, A. G.	Murphy, R. A.*	Ward, J. H. R., III
Caswell, F. H.	Hinkley, E. D.	Norris, P. E.†	Wolfe, C. M.
Clough, T. F.	Hurwitz, C. E.	Oliver, M. R.*	Youtz, P.
Donaldson, P. L.	Lindley, W. T.		

*Research Assistant

†Summer Staff

‡Part Time



REPORTS BY AUTHORS ENGAGED IN SOLID STATE RESEARCH

15 May through 15 August 1967

PUBLISHED REPORTS

Technical Notes

TN No.			<u>DDC and Hayden Nos.</u>
1967-15	A Theorem on Spin-Eigenfunctions	T. A. Kaplan W. H. Kleiner	24 May 1967 DDC 652840 H-849

Journal Articles*

JA No.			
2602	Introduction to the Theory of Exciton States in Semiconductors	J. O. Dimmock	<u>Semiconductors and Semimetals</u> , Vol. 3 (Academic Press, New York, 1967)
2811	Superconducting Transition Temperature and Electronic Structure in the Pseudobinaries Nb ₃ Al-Nb ₃ Sn and Nb ₃ Sb-Nb ₃ Sb	F. J. Bachner† J. B. Goodenough H. C. Gatos†	J. Phys. Chem. Solids <u>28</u> , 889 (1967)
2850	High-Temperature Expansions for the Classical Heisenberg Model. I. Spin Correlation Function	H. E. Stanley	Phys. Rev. <u>158</u> , 537 (1967)
2891	New Phase Transformation in InSb at High Pressure and High Temperature	M. D. Banus M. C. Lavine	J. Appl. Phys. <u>38</u> , 2042 (1967)
2900	Quantum Kinetic Equations for Electrons in Random Impurities	P. N. Argyres E. S. Kirkpatrick*	Ann. Phys. <u>42</u> , 513 (1967)
2907	High-Temperature Expansions for the Classical Heisenberg Model. II. Zero-Field Susceptibility	H. E. Stanley	Phys. Rev. <u>158</u> , 546 (1967)
2909	High-Pressure Study of the First-Order Phase Transition in MnAs	J. B. Goodenough J. A. Kafalas	Phys. Rev. <u>157</u> , 389 (1967)

* Reprints available.

† Author not at Lincoln Laboratory.

Reports

JA No.

2941	Retrograde Solubility in n-Type PbS	A. J. Strauss	Trans. Met Soc. AIME <u>239</u> , 794 (1967)
2955	Photo and Thermal Effects in Compensated Zinc-Doped Germanium	R. J. Keyes	J. Appl. Phys. <u>38</u> , 2619 (1967)
2962	GaAs-InSb Graded-Gap Hetero-junction	E. D. Hinkley R. H. Rediker*	Solid-State Electron. <u>10</u> , 671 (1967)
2963A	Inversion of Conduction and Valence Bands in $Pb_{1-x}Sn_x$ Alloys	A. J. Strauss	Phys. Rev. <u>157</u> , 608 (1967)
2967	Landau Damping of Magneto-plasma Waves for General Closed Fermi Surfaces	A. L. McWhorter J. N. Walpole*	Phys. Rev. <u>158</u> , 719 (1967)
2968	Nonlocal Effects in Low-Field Helicon Propagation in PbTe	J. N. Walpole* A. L. McWhorter	Phys. Rev. <u>158</u> , 708 (1967)
2975	Report on the Seventh International Conference on the Physics of Semiconductors	B. Lax* J. G. Mavroides	Phys. Today <u>20</u> , 101 (1967)
2978	Magnetoplasma Cyclotron Absorption in PbSe	S. Bermon	Phys. Rev. <u>158</u> , 723 (1967)
2993	Magnetic and Structural Study of the Spinel $MnYb_2S_4$	J. M. Longo P. M. Raccach	Materials Res. Bull. <u>2</u> , 541 (1967)
2994A	Stability Measurements of CO_2-N_2-He Lasers at 10.6 μm Wavelength	C. Freed	IEEE J. Quant. Electron. <u>QE-3</u> , 203 (1967)
3018	Growth of Single Ti_2O_3 Crystals from the Melt	T. B. Reed R. E. Fahey J. M. Honig	Materials Res. Bull. <u>2</u> , 561 (1967)
3023	Laser Emission from Electron Beam Excited ZnTe	C. E. Hurwitz	IEEE J. Quant. Electron. <u>QE-3</u> , 333 (1967)
3026	Stimulated Raman Scattering in an Infrared Active, Non-totally Symmetric Vibration of α -Quartz	P. E. Tannenwald D. L. Weinberg*	IEEE J. Quant. Electron. <u>QE-3</u> , 334 (1967)
3052	Low-Energy Interband Transitions and Band Structure in Nickel	J. Hanus J. Feinleib W. J. Scouler	Phys. Rev. Letters <u>19</u> , 16 (1967)
MS-1629A	Narrow Band Electrons in Transition-Metal Oxides	J. B. Goodenough	Czech. J. Phys. <u>B17</u> , 304 (1967)

* Author not at Lincoln Laboratory.

UNPUBLISHED REPORTS

Journal Articles

JA No.

3021	Localized vs Collective d Electrons and Neel Temperatures in Perovskite and Perovskite-Related Structures	J. B. Goodenough	Accepted by Phys. Rev.
3025	InSb-GaAsP Infrared to Visible Light Converter	R. J. Phelan, Jr.	Accepted by Proc. IEEE
3066	Magnetic Interactions and Spiral Ground States in Spinels, with Application to ZnCr_2Se_4	K. Dwight N. Menyuk	Accepted by Phys. Rev.
3068	Theory of the Magnetic Properties of the Ilmenites MTiO_3	J. B. Goodenough J. J. Stickler	Accepted by Phys. Rev.
3069	Magnetic Resonance and Sus- ceptibility of Several Ilmenite Powders	J. J. Stickler G. S. Heller* S. Kern* A. Wold*	Accepted by Phys. Rev.
3070	Tetrahedral-Site Copper in Chalcogenide Spinels	J. B. Goodenough	Accepted by Solid State Commun.
3074	A 10.6 Micron 4 Port Circu- lator Using Free Carrier Rotation in InSb	J. H. Dennis	Accepted by J. Quant. Electron.
3076	Spark Source Mass Spectroscopy	E. B. Owens	Accepted by 1968 McGraw-Hill Yearbook of Science and Tech- nology
3080	Current Runaway and Avalanche Effects in n-CdTe	M. R. Oliver A. L. McWhorter A. G. Foyt	Accepted by Appl. Phys. Letters
3085	Observation of Exciton Fine Structure in the Interband Magnetabsorption of InSb and Germanium	E. J. Johnson	Accepted by Phys. Rev. Letters
3086	The Gunn Effect in n-CdTe	M. R. Oliver A. G. Foyt	Accepted by IEEE Trans. Electron Devices
3087	Inversion Asymmetry Effects on Oscillatory Magnetoresistance in HgSe	L. M. Roth* S. H. Groves P. W. Wyatt*	Accepted by Phys. Rev. Letters

* Author not at Lincoln Laboratory.

Reports

JA No.

- | | | | |
|------|---|---|---------------------------------|
| 3090 | New Expansions for Classical Heisenberg Model and Similarity to $S = 1/2$ Ising Model | H. E. Stanley | Accepted by Phys. Rev. |
| 3091 | Electroreflectance Study of Interband Magneto-Optical Transitions in InAs and InSb at 1.5°K | C. R. Pidgeon*
S. H. Groves
J. Feinleib | Accepted by Solid State Commun. |
| 3097 | Perturbation Calculation of Band Structure Effects in Low-Field Helicon Propagation | A. L. McWhorter
J. N. Walpole* | Accepted by Phys. Rev. |

Meeting Speeches†

MS No.

- | | | | |
|-------|--|------------------|--|
| 1629D | Structure and Magnetism in Transition Metal Compounds | J. B. Goodenough | Seminar, Worcester Polytechnic Institute, 15 May 1967 |
| 1747A | On the Possible Phase Transitions for Two-Dimensional Heisenberg Models | H. E. Stanley | Seminar, Case Institute of Technology, 19 - 23 June 1967 |
| 1896 | A Carbon Dioxide Laser Radar System | H. A. Bostick | } Conference on Laser Engineering and Application, Washington, D.C., 6 - 9 June 1967 |
| 1913 | Stability Measurements of CO ₂ -N ₂ -He Lasers at 10.6 μm Wavelength | C. Freed | |
| 1919A | Properties and Applications of Small-Bandgap Pb _{1-x} Sn _x Te and Pb _{1-x} Sn _x Se | I. Melngailis | Seminar, NASA Electronic Research Center, Cambridge, Massachusetts, 31 May 1967 |
| 1950 | Structural and Magnetic Consequences of Peculiar Chemical Bonding in PbRuO ₃ and FeRh | J. B. Goodenough | International Symposium on Problems of Chemical Bonding in Semiconductor Crystals, Minsk, U.S.S.R., 28 May - 3 June 1967 |
| 1963A | Quantum Kinetic Equations for Electrons in Random Impurities | P. N. Argyres | U. S. Naval Ordnance Laboratory, Silver Spring, Maryland, 16 May 1967 |

* Author not at Lincoln Laboratory.

† Titles of Meeting Speeches are listed for information only. No copies are available for distribution.

MS No.

1971	Mode Structure in a Resonant Raman Oscillator	P.E. Tannenwald	American Physical Society, Toronto, Canada, 21 - 23 June 1967
1972	Wide Range Continuously Tunable High Power Sum Frequency Generation	R.L. Carman	
2007	Dynamics of Intense Light Beams in Nonlinear Media	P.L. Kelley	
1976A	The Evolution of Intense Short Pulses in Nonlinear Optical Media	T.K. Gustafson* F. DeMartini* C.H. Townes* P.L. Kelley	Electron Devices Research Conference, McGill University, 21 - 23 June 1967
1999	Thermodynamics of Optical Pulse Interactions	H.A. Haus* P.L. Kelley T.K. Gustafson*	
1980	Modern High Pressure Techniques	J.A. Kafalas	High Pressure Treatment of Ma- terials, ManLabs, Incorporated, Cambridge, Massachusetts, 18 - 19 May 1967
2015	Survey of Equipment for High Pressure Studies	M.D. Banus	
2016	Retained High Pressure Phases and High Pressure Synthesis	M.D. Banus	
1986	$Pb_{1-x}Sn_x$ Diode Lasers	J.F. Butler T.C. Harman	Solid State Device Research Conference, University of California, 19 - 21 June 1967
1987	Photovoltaic Response of $Pb_{1-x}Sn_x$ Diodes	A.R. Calawa I. Melngailis T.C. Harman J.O. Dimmock	
1989	Epitaxial Gallium Arsenide for Gunn Effect Oscillators	C.M. Wolfe A.G. Foyt W.T. Lindley	
1991, 1991A	Anomalous 18cm Absorption and Emission of Interstellar OH	M.M. Litvak	Seminar, M.I.T., 2 June 1967; American Astronomical Society, Yerkes Observatory, Williams Bay, Wisconsin, 12 - 15 June 1967
1996A	Electron-Beam-Pumped Lasers of II-VI Compound Semiconductors	C.E. Hurwitz	Seminar, IBM Watson Research Laboratory, Yorktown Heights, New York, 16 June 1967
2023	Electron Band Structure Studies Using Differential Optical Techniques and High Magnetic Fields	J.G. Mavroides	Physics of Solids in Intense Magnetic Fields, Crete, Greece, 16 - 29 July 1967

* Author not at Lincoln Laboratory.

Reports

MS No.

2025	Magneto spectroscopy	J. G. Mavroides	Seminar, Demokritos, Athens, Greece, 31 July 1967
2032	Plasmas for Material Preparation and Crystal Growth	T. B. Reed	} Summer Course in Crystal Growth, M.I.T., 10 - 21 July 1967
2033	Vapor Growth of Crystals	T. B. Reed	
2039	High-Temperature Expansion of the Zero-Field Susceptibility for the Classical Heisenberg Model	H. E. Stanley	School of Physics, Santiago, Chile, 17 - 28 July 1967
2065	Conduction Processes in Oxides	J. B. Goodenough	Gordon Conference, Andover, New Hampshire, 17 - 21 July 1967
2067, 2067A	High Pressure Studies on Some Intermetallic Compounds and Defect-Structure Metallic Oxides	M. D. Banus	Batelle Memorial Institute, Richland, Washington, 1 August 1967; Lawrence Radiation Laboratory, University of California, 3 August 1967

I. SOLID STATE DEVICE RESEARCH

A. $\text{Pb}_{1-x}\text{Sn}_x\text{Se}$ PHOTOVOLTAIC DETECTORS

The variation of detection efficiency with depth of the p-n junction was determined for $\text{Pb}_{1-x}\text{Sn}_x\text{Se}$ photovoltaic detectors by repeated etching to reduce the junction depth. Figure I-1 is a plot of detector efficiency (η) at a wavelength of 4.2μ as a function of junction depth (d) for two $\text{Pb}_{0.933}\text{Sn}_{0.067}\text{Se}$ diodes at 77°K . At the 4.2μ wavelength the photon energy is sufficiently above the bandgap so that all of the radiation is absorbed very close to the surface. Under this condition it can be shown that the detector efficiency, defined as the number of minority carriers which reach the p-n junction per incident photon, is given approximately by

$$\eta = 2(1-R) \left(1 + \frac{s\tau}{L}\right)^{-1} e^{-d/L} \quad \text{for } d > L.$$

Here η is the efficiency, R the reflectivity, s the surface recombination velocity, τ the minority carrier lifetime, L the minority carrier diffusion length and d the junction depth.

Both diodes shown here were from the same $\text{Pb}_{0.933}\text{Sn}_{0.067}\text{Se}$ crystal and from the same diffusion. Their initial junction depth was 14μ . Note that the greatest increase in efficiency

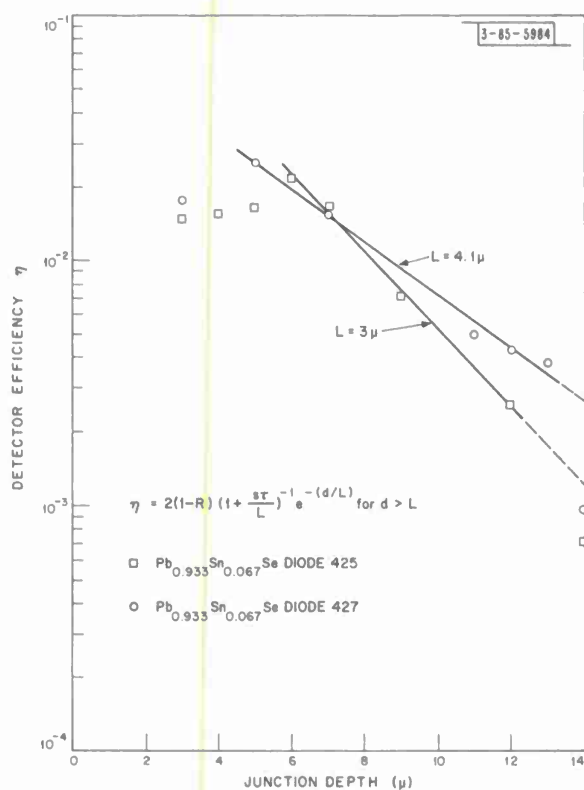


Fig. I-1. Dependence of detection efficiency on junction depth in two $\text{Pb}_{0.933}\text{Sn}_{0.067}\text{Se}$ diodes.

occurred after the initial etch. This suggests that the etched surface has a reduced surface recombination velocity. The data then follows the expected logarithmic variation to a depth of about 5μ after which both devices exhibit a decrease in efficiency. This can be caused by an increase in spreading resistance about the contact, resulting in an effective decrease in surface area or an actual decrease in effective area due to feathering of the surface layer at the edges of the junction. From the linear portion of these curves we deduce diffusion lengths of 3 and 4μ for the two diodes.

The speed of response of a number of detectors was measured by using a GaAs laser diode as a fast light source. The detector response times ranged from less than 5 to 100 nsec. To determine the mechanism which limits the speed, the capacitance of the diodes was measured by using a capacitance bridge at 20 MHz. The capacitance was typically 2000 pf/mm^2 . The RC time constant of the diodes ranged between 1 and 5 nsec. In most of the cases examined, the response speed of

Section I

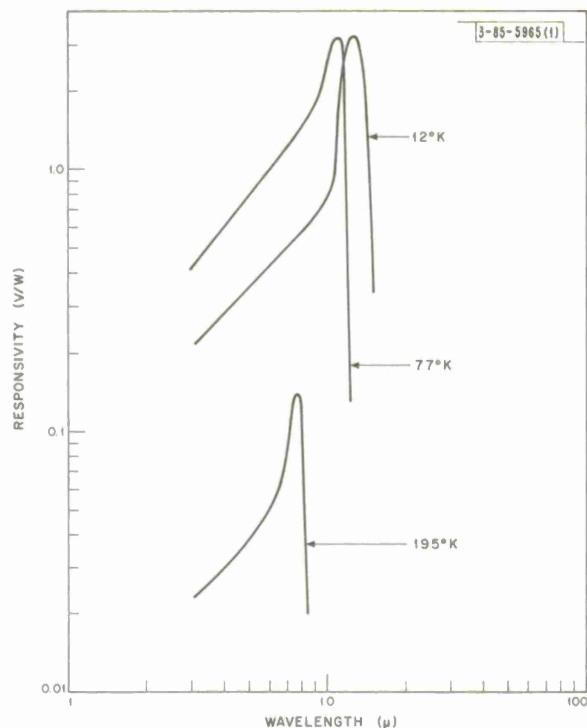


Fig. I-2. Responsivity spectra of a $\text{Pb}_{0.936}\text{Sn}_{0.064}\text{Se}$ diode at 12°, 77° and 195°K.

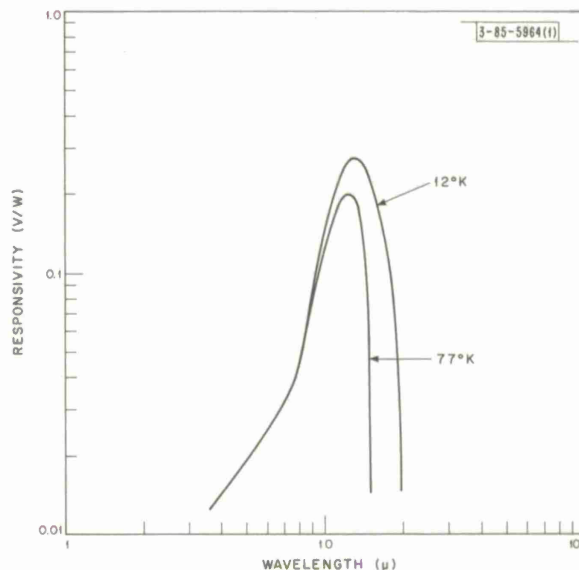


Fig. I-3. Responsivity spectra of a graded gap $\text{Pb}_{1-x}\text{Sn}_x\text{Se}$ diode.

the detectors was not RC-limited, but was probably limited by the effective lifetime of the minority carriers. Further evidence for this was provided by the observation that the response speed of some detectors was greatly reduced by etching the surface. This is consistent with a decrease in surface recombination velocity, which provides a mechanism for the recombination of the carriers stored in the region between the surface and the junction.

Responsivity spectra of a number of detectors were measured at 195°K, the temperature of dry ice. As shown in Fig. I-2, the cutoff wavelength is 8.5μ at 195° for a detector whose cutoff at 12°K is 15μ and 12μ at 77°K. Whereas the peak responsivity is about 3 V/W both at 12°K and at 77°K, a decrease by a factor of 20 occurs as the temperature is increased to 195°K.

Some detectors were made from $\text{Pb}_{1-x}\text{Sn}_x\text{Se}$ wafers which had a graded bandgap near the surface, resulting from a change in the Sn content in the process of annealing. Figure I-3 shows the responsivity of a detector made from a graded gap material in which the SnSe content varies from 8.7 percent at the surface to 12.5 percent at a depth of 13μ . The resulting bandgap variation at 77°K is from 0.09 eV at the surface to 0.07 eV in the bulk. The cutoff wavelength determined by the bandgap energy near the junction is 15μ at 77°K and 20μ at 12°K. The junction depth was approximately 8μ and the surface was not etched. The responsivity of this detector has a peak prior to cutoff but the peak is considerably broader and the cutoff more gradual than for the detector in Fig. I-2, which does not have a graded bandgap.

A. R. Calawa
I. Melngailis

B. $\text{Pb}_{1-x}\text{Sn}_x\text{Se}$ DIODE LASERS

$\text{Pb}_{1-x}\text{Sn}_x\text{Se}$ diode lasers have been fabricated with output powers as high as 80 mW and external quantum efficiencies of up to 5 percent. The crystals used in these devices were grown either by the Bridgman method or by vapor phase transport. Slices of the Bridgman-grown crystals were annealed under a controlled atmosphere to obtain low carrier concentration and high mobility. The material used for lasers had carrier concentrations in the low 10^{17} cm^{-3} range and 77°K Hall mobilities in excess of $20,000 \text{ cm}^2 \text{ V}^{-1} \text{ sec}^{-1}$. We have used both p- and n-type starting material and have noticed no significant difference in the laser properties. P-N junctions were formed by the method previously used for PbSe diodes,¹ that is, an excess of metal was diffused into the surface of p-type material and an excess of Se into n-type crystals. The diffusions were done in a closed tube using for a vapor source a coarsely ground ingot of $\text{Pb}_{1-x}\text{Sn}_x\text{Se}$ with the Sn content of the sample and with an excess of $\text{Pb}_{1-x}\text{Sn}_x$ or Se. Junction depths were generally 10 to 20 μ . The diffusions were made into [100] surfaces. After the diffusions, lasers were formed by cleaving along the perpendicular [100] surfaces. Ohmic contact was made with Ag to the p-side and In to the n-side. The lasers were mounted in low inductance packages using room temperature bonding techniques. Typical laser dimensions were $200 \times 400 \mu$ in cross section and 100 μ in thickness. Since all six faces of the laser were cleaved, the long sides had to be rendered nonreflecting. This was done with a severe etch in a solution of potassium hydroxide, hydrogen peroxide and ethylene glycol. This step is necessary to achieve maximum power output.

Figure I-4 shows spectra for a $\text{Pb}_{0.945}\text{Sn}_{0.055}\text{Se}$ laser at 12°K. Below threshold the emission intensity increases very rapidly with current. The threshold current was about 950 A cm^{-2} for this laser. The spectrum above threshold is resolution-limited. The line width is less than 10^{-5} eV . This particular device showed essentially single-mode operation to current levels well above threshold. The beam angle in the plane of the junction was only about 1.5° , indicating that nearly the entire 500- μ wide face of the diode was emitting. In the vertical direction the angle was limited by the package but was at least 30° , indicating that the width of the emitting region in this direction was less than 27 μ .

Figure I-5 shows a laser spectrum for a diode with 8 percent SnSe. This emission at 18.8 μ is at present the long wavelength limit for unstressed semiconductor lasers.

Peak emission power measurements were made by observing the output of a calibrated Cd-doped Ge detector directly on an oscilloscope. At high power levels the measurements were checked with a calibrated thermopile. Figure I-6 shows peak output power as a function of diode current for a $\text{Pb}_{0.945}\text{Sn}_{0.055}\text{Se}$ laser at 12°K. The diode was pulse-biased at a duty cycle of 10^{-4} . Threshold current density for this laser was about 500 A cm^{-2} . The maximum power of 80 mW corresponds to an external quantum efficiency of about 5 percent. The output power continues to rise superlinearly, even at the highest power levels. This indicates that the internal quantum efficiency has not attained its limiting value and that the power output for this diode is limited by some competing recombination process. Earlier photoluminescence² studies of the Pb salts have indicated that nonradiative recombination occurs at lattice defects in these semiconductors.

Section I

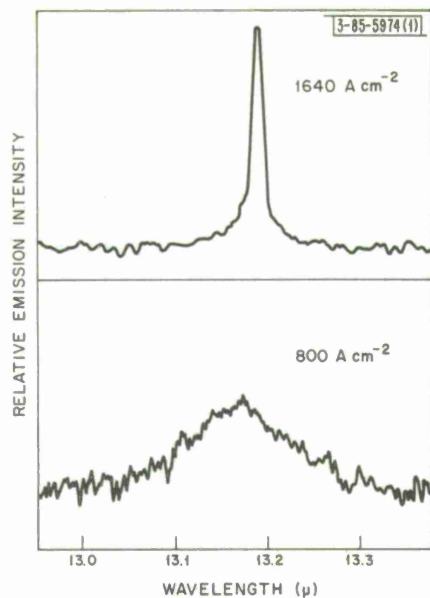


Fig. 1-4. Emission spectra of a $\text{Pb}_{0.945}\text{Sn}_{0.055}\text{Se}$ diode laser at 12°K.

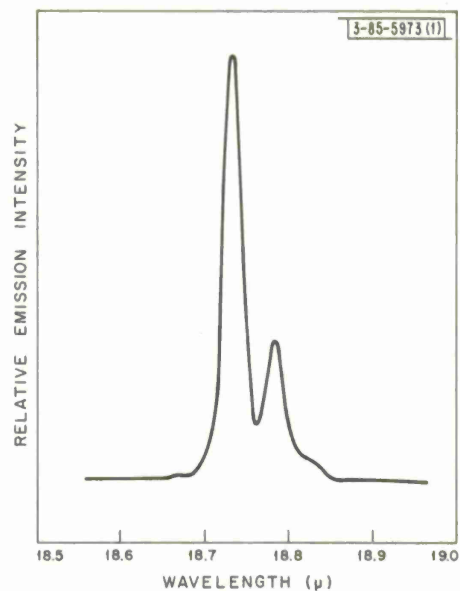


Fig. 1-5. Emission spectrum of a $\text{Pb}_{0.920}\text{Sn}_{0.080}\text{Se}$ diode laser at 12°K.

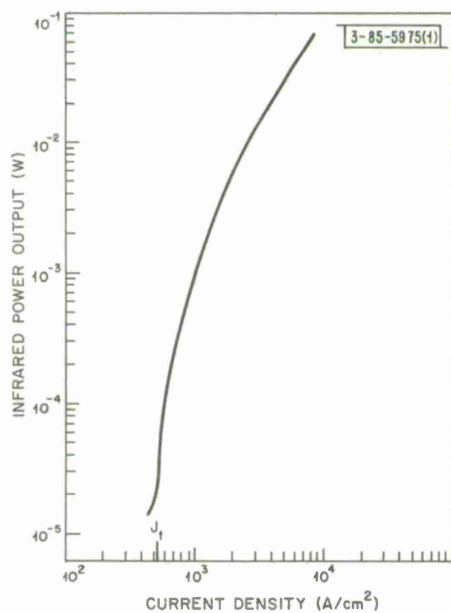


Fig. 1-6. Peak power output of a pulsed $\text{Pb}_{0.945}\text{Sn}_{0.055}\text{Se}$ diode laser at 12°K.

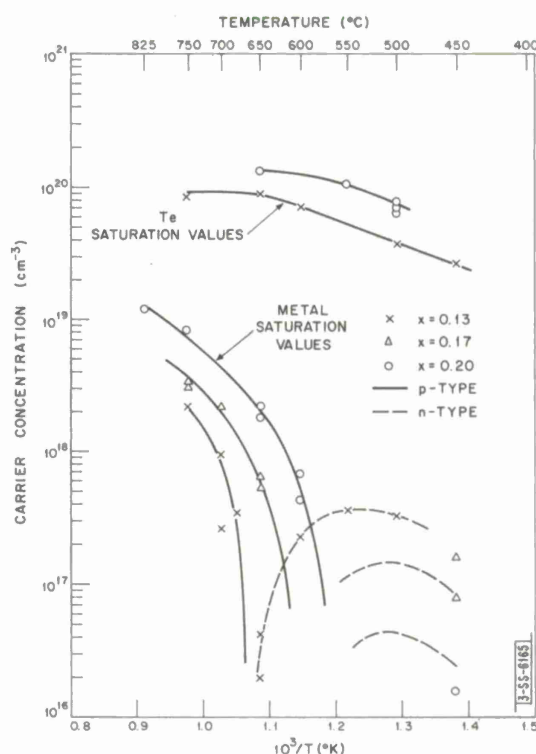
Threshold current densities at 12°K have been between 500 and 1000 A cm⁻² for all the Pb_{1-x}Sn_xSe lasers tested. At 77°K, threshold current densities ranged from 2400 A cm⁻² to over 30,000 A cm⁻². No definite correlation between threshold currents at the two temperatures has been noted. The power output at 77°K in the low threshold current devices is of the same order of magnitude as that at 12°K.

J. F. Butler
T. C. Harman

C. ISOTHERMAL ANNEALING OF Pb_{1-x}Sn_xTe

In the previous report,³ isothermal annealing experiments for Pb_{1-x}Sn_xTe with x = 0.20 were reported. Low carrier concentration crystals were obtained by using 0.25-mm thick samples, long annealing times and low annealing temperatures. In this quarter, the annealing

Fig. 1-7. Carrier concentration vs temperature for metal-saturated and Te-saturated Pb_{1-x}Sn_xTe, which has been isothermally annealed.



experiments were extended to the additional compositions, x = 0.13 and x = 0.17, to various temperatures, and to both metal-saturated and Te-saturated conditions. The solidus lines for the Te-rich side of the phase diagram are shown in Fig. 1-7 as the upper two curves. The hole carrier concentrations are seen to be very large. The lower three curves in the figure are for the metal-saturated condition. For x = 0.13, the solidus line in equilibrium with metal-rich material is on the Te-rich side of the stoichiometric composition above approximately 660°C and on the metal-rich side below this temperature. For x = 0.17, the crossover appears to be slightly above 600°C. Electron carrier mobilities were as large as 40,000 cm²/volt-sec at 77°K and a number of crystals with carrier concentrations in the 10¹⁶/cm³ range were measured.

T. C. Harman

D. HIGH POWER AND EFFICIENCY IN CdSe ELECTRON-BEAM-PUMPED LASERS

Pulsed electron-beam-pumped lasers prepared from single crystal platelets of CdSe grown* in an atmosphere of excess Cd have yielded values of output power and efficiency considerably greater than observed previously⁴ in CdSe and comparable to those obtained recently⁵ in similarly grown crystals of CdS. At 4.2° with a 60 keV beam, 300 W of peak output power and an overall power efficiency of 28 percent have been measured. The latter figure, when corrected for losses due to electron backscattering^{6,7} and optical absorption in the evaporated aluminum reflective layer,⁸ yields an internal power conversion efficiency of 38 percent. With increasing temperature, the performance of the lasers fell off more rapidly than was the case in CdS. At 77°K, the maximum measured values of peak power, overall efficiency, and internal efficiency were 184 W, 19 percent, and 25 percent, respectively. No lasing was observed at temperatures above approximately 100°K. Minimum observed threshold beam currents with 60 keV excitation were 70 μ A at 4.2°K and 360 μ A at 77°K.

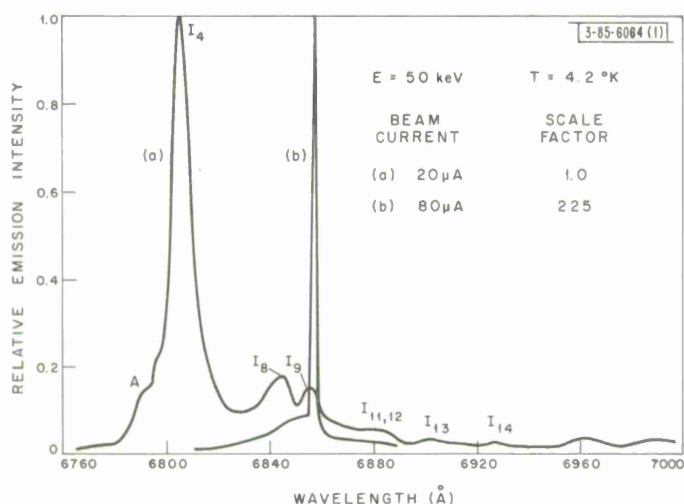


Fig. I-8. Emission spectra of Cd-rich CdSe below and above laser threshold.

A typical set of emission spectra below and above the laser threshold is shown in Fig. I-8. Note the intensity scale factors. The notations on the major spontaneous lines correspond to those used by Reynolds, *et al.*,⁹ to denote the same or similarly located lines observed in photoluminescence. Note that the strong I_5 and I_6 lines reported by Reynolds and co-workers are apparently missing from the present spectra. It is conceivable that the Cd-rich growth suppresses these lines as it does the I_4 line in CdS.⁵ The spectrum as shown has been shifted about 3 Å toward longer wavelengths to bring the position of the lines into coincidence with those observed by the above authors. In many of the electron-beam-excited samples of CdSe, as well as those of CdS, the overall spectra, when compared to similar photoluminescence spectra, are found to be translated toward shorter wavelengths by as much as 10 Å, the amount of the shift varying from sample to sample. This shift is attributed to strain introduced in cooling the

*These platelets were grown by D. C. Reynolds of the Aerospace Research Laboratory, Wright-Patterson Air Force Base, Ohio.

samples, one whole surface of which is firmly attached to a copper heat sink, in contrast to the relatively strain-free mounting used in photoluminescence experiments.

As indicated in Fig. I-8, the laser emission in CdSe arises in the vicinity of the line (or lines) denoted by I_9 , although in other crystals laser emission has also been observed from the region of the line I_8 . It has been suggested by Reynolds, *et al.*,⁹ that the lines I_8 and I_9 could result from the Auger recombination of an exciton bound to a neutral center, wherein, after the decay of the exciton, the center is left in an excited state. However, one would expect that as is the case in GaP (Ref. 10), the lines resulting from these "two electron" transitions would occur in all samples with approximately the same intensity relative to a line resulting from the simple decay of the pertinent bound exciton. Our results do not yield such a relationship, thus indicating that either the simple model is incorrect or that the lines in the Cd-rich samples, from which laser emission occurs, are not the same as the similarly located I_8 and I_9 lines referred to by Reynolds, *et al.*

In Cd-rich CdS, Litton and co-workers* have recently observed several strong emission lines in the vicinity of 4900 Å which they have attributed to recombination of excitons bound to donor-acceptor complexes. One of these lines, occurring at 4895 Å is very likely the same line which we have observed at 4897 Å from which the laser emission arises.⁵ In view of the similarity between CdSe and CdS, it would be reasonable to suppose that the mechanism for efficient laser emission is the same in both materials.

C. E. Hurwitz

E. EPITAXIAL GALLIUM ARSENIDE FOR GUNN EFFECT OSCILLATORS

Recently, we have reported results on high efficiency Gunn oscillators (9 percent at 10 GHz) which were fabricated from epitaxial layers grown by the AsCl_3 -Ga- H_2 flow system.¹¹ In this report we discuss details of the materials preparation process which we have found to be important for obtaining reproducible high quality material and high efficiency devices.

1. Epitaxial Process

A diagram of the epitaxial reactor is shown in Fig. I-9. The high temperature part of the system including the Ga boat and the seed holder is fabricated from high-purity synthetic quartz. The AsCl_3 bubbler is made of quartz and Teflon gas lines are used. Prior to use, the entire system is cleaned and baked out under high vacuum.

The reaction proceeds as follows: Pd purified H_2 is metered through the liquid AsCl_3 and a by-pass dilution line. The H_2 is saturated with AsCl_3 in the bubbler and, together with the by-pass H_2 , passes into the hot furnace where the AsCl_3 is reduced by the H_2 . At the Ga boat, Ga chlorides are formed and As is almost completely absorbed by the Ga until equilibrium is reached. At this time, As proceeds to the lower temperature seed zone where it reacts with the Ga deposited by the disproportionation reaction between the Ga chlorides to form an epitaxial layer on the seeds. Quantitatively, the growth conditions are: H_2 flow through the AsCl_3 100 ml/min., H_2 by-pass flow 150 ml/min., Ga temperature 850°C, seed etching temperature 850 to 900°C, seed growth temperature 750°C, and a seed temperature gradient of about 20°C/in. By the use of a temperature gradient, layer thickness can be controlled to about ± 10 percent.

*C. W. Litton, D. C. Reynolds and T. C. Collins, paper to be presented at International Conference on II-VI Semiconducting Compounds, Providence, R. I., September 1967.

Section I

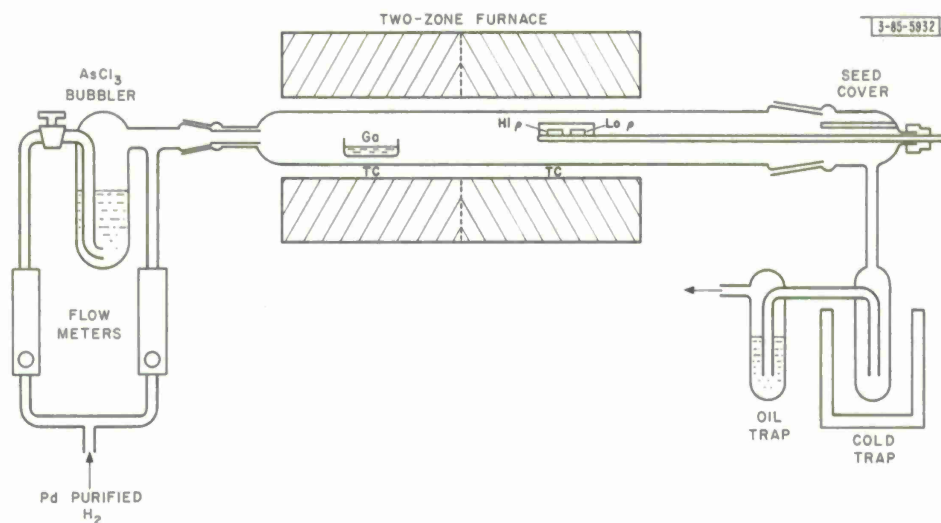


Fig. 1-9. Epitaxial reactor.

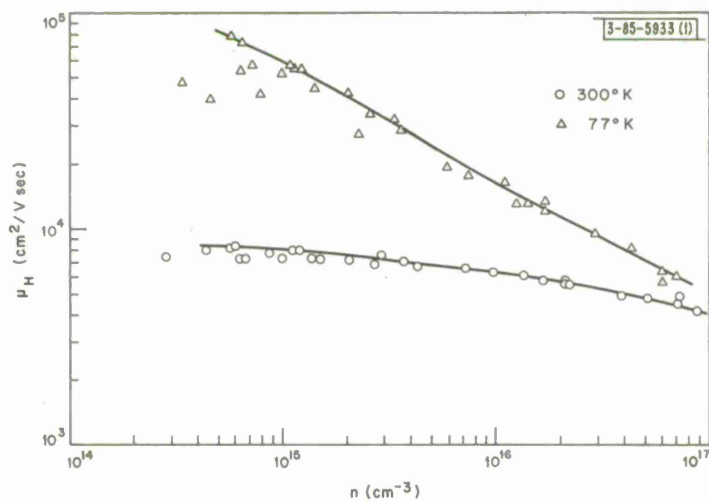


Fig. 1-10. Hall mobility vs carrier concentration at 300 and 77°K (measurements at 10kG).

Usually, two seeds are used: a high-resistivity substrate for Hall measurements and a low-resistivity substrate for device fabrication. Before insertion in the epitaxial reactor, the seeds are mechanically-chemically polished with NaOCl on a Pellum cloth, polish-etched with a solution of five parts H_2SO_4 , one part H_2O and one part H_2O_2 for 10 minutes, soaked in a chelating agent (Na salt of EDTA) for 30 minutes, and rinsed in a transistor washer. Prior to growth the seeds are vapor etched in the reactor to insure good crystalline layers. During the furnace heat-up cycle, the Ga saturation process, and the furnace cool-down cycle, the seeds are left out of the furnace in a quartz box (the seed holder and a cover) to protect them from the reaction products. The resultant epitaxial layers have smooth interfaces and are crystallographically sound.

2. Electrical Measurements

The Hall mobility of layers obtained with this system is shown in Fig. I-10 as a function of carrier concentration. Measurements were made by the van der Pauw¹² method on high-resistivity Cr-doped seeds. A magnetic field of 10 kG was used to approach the high-field limit.¹³ With this field, the mobility at 300°K increases with decreasing carrier concentration to about $8500 \text{ cm}^2/\text{V sec}$ while at 77°K it increases to about $80,000 \text{ cm}^2/\text{V sec}$. The scatter in 77°K mobility below $n = 10^{15} \text{ cm}^{-3}$ is due to a variation in compensation at this low level. Carrier concentrations from about 3×10^{14} to $3 \times 10^{15} \text{ cm}^{-3}$ were obtained with residual impurity doping while higher values were obtained with donor impurities in the Ga boat.

We have found that good electrical properties are easy to obtain with this system using commercially available AsCl_3 and Ga. Given good-quality starting material, the main problem we have encountered in obtaining GaAs with good electrical properties has been small air leaks in the input lines which produce high resistivity or heavily compensated material.

3. Device Problems

High mobility GaAs, however, is a necessary but not a sufficient condition for the production of good devices. When devices are made from layers deposited on heavily doped seeds, other problems become apparent which affect device reproducibility and degrade their performance.

Two problems which can be encountered are: widely differing resistivities for devices made from the same epitaxial layer, and low-field nonohmic characteristics not related to contact effects. We have found that the use of the chelating agent in surface preparation reduces these problems considerably. The chelating agent removes adsorbed impurities from the substrate surface. However, even when the chelating agent is used, nonohmic devices and devices which cannot be biased to sufficiently high electric fields without producing an avalanche type of breakdown have resulted from layers grown on Si-doped seeds. We believe that in this case an impurity gradient is formed in the epitaxial layer as a result of the outdiffusing substrate dopant.

To examine these problems, impurity profiles of the epitaxial layers were determined by differential capacitance measurements on reverse-biased Schottky barrier diodes.

4. Differential Capacitance Measurements

Schottky barrier diodes on the epitaxial layers were constructed as shown in Fig. I-11. The diodes were prepared by depositing pyrolytic silicon dioxide on the epitaxial surface, etching photolithographically determined holes in the oxide, and electroplating Au through the holes.

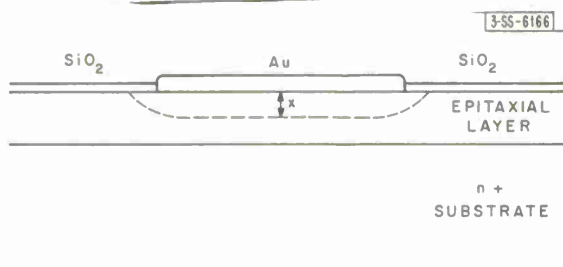


Fig. I-11. Schottky barrier diode.

The equations used to determine the impurity concentration $N(x)$ at a given depletion layer width x are,

$$N(x) = \frac{C^3}{e\epsilon A^2(-dC/dV)} \quad \text{and} \quad x = \frac{\epsilon A}{C}$$

where A is the area of the diode.¹⁴ To minimize error, measurements were taken so that $\Delta C/C = 1/10$ (Ref. 15).

In order to profile the entire layer thickness, the Au barriers were removed, the sample was etched through the holes in the SiO_2 , the Au was replaced, and the measurement repeated. The etching process was calibrated by overlapping profiles. In the following figures the various etch depths are indicated by vertical dotted lines.

5. Impurity Profiles

The impurity profiles of two layers, both about 10μ thick and both grown on Si-doped substrates, are shown in Fig. I-12. Low field nonohmic current-voltage characteristics were

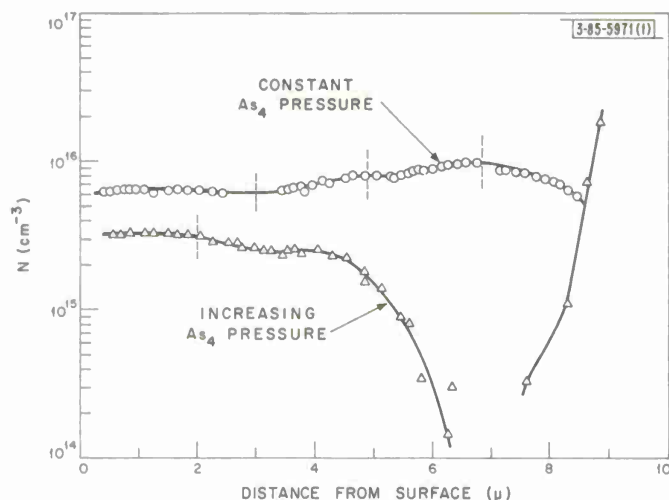


Fig. I-12. Impurity profiles of epitaxial layers grown on Si-doped substrates under different growth conditions.

observed for all devices made from these layers. The interface of the upper profile has not been completely resolved. These layers were prepared in the same manner except that the growth of the layer corresponding to the steeper profile was initiated in a vapor with a low As pressure, most of the As still being absorbed in the Ga boat. The growth of the layer with the relatively flat profile was initiated with a higher As pressure and relatively constant Ga-to-As ratio, corresponding to complete saturation of the Ga boat.

We attribute the difference in the two curves to the effect of the As pressure on the incorporation on Ga and As lattice sites of the Si which outdiffuses from the substrate. In this case, as the As pressure increases, fewer Si atoms are incorporated on As sites (producing Si acceptors) and a flatter profile is obtained.

When growth is initiated under a low As pressure, the profiles are quite different for layers grown on substrates doped with column IV and column VI elements. Figure I-13 shows the profiles of two epitaxial layers grown using the same starting materials, with the same residual impurity doping, and identical processing. The upper profile corresponds to a layer grown on a Te-doped seed, while the lower profile corresponds to a layer grown on a Si-doped seed. In both cases, growth was initiated under a low As pressure. For the upper profile, a long diffusion tail above the system doping level is observed from the Te-doped substrate, while for the lower curve corresponding to the Si-doped substrate, a region is observed below the residual impurity doping. Both of these profiles can be explained if we assume that the low As pressure enhances the incorporation of the outdiffusing Te and Si on As sites. In the first case, the doping near the seed is higher than the background level, while in the second the doping is lower near the seed.

The material with the relatively flat profile yielded good devices, while devices from material with the dip near the seed did not oscillate, and exhibited current runaway at moderate fields. Poor device performance has also been observed for impurity gradients produced by other means, such as variations in intentional doping. We have found this to be the most obvious difference between good and poor device-quality material produced with this process.

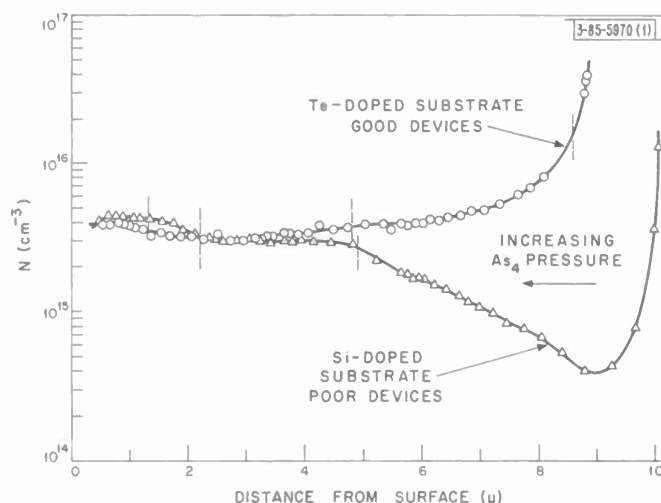


Fig. I-13. Impurity profiles of epitaxial layers grown under same conditions for different substrate dopants.

Section I

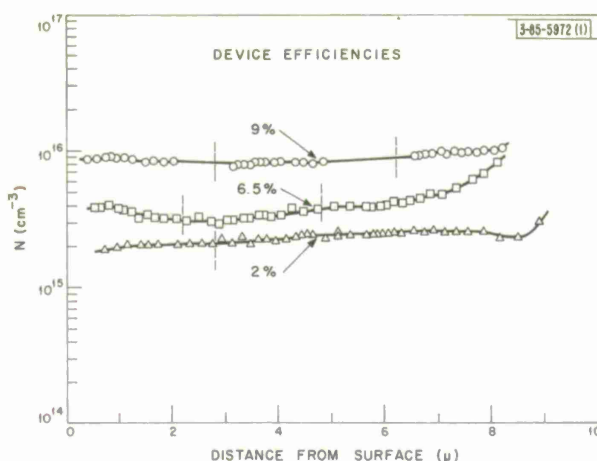


Fig. I-14. Impurity profiles of epitaxial layers giving good devices.

Figure I-14 shows the impurity profiles of three epitaxial layers which reproducibly yielded good devices at about 10 GHz. All have a fairly uniform profile. Carrier concentrations obtained from Hall measurements on control seeds and from differential capacitance measurements on device seeds are in good agreement. The two lower curves correspond to layers grown from source materials which were not intentionally doped. The layer corresponding to the upper profile was intentionally doped by introducing Ge in the Ga boat.

6. Conclusions

If the Ga is not completely saturated with As before growth begins, large impurity gradients are obtained in the epitaxial layer. These gradients are produced by an interaction between the As vapor and the outdiffusing seed dopant. The gradients obtained with Si-doped seeds are particularly detrimental to device performance. By proper consideration of these problems, reproducible material for high-efficiency Gunn oscillators can be obtained with this system.

C. M. Wolfe
A. G. Foyt
W. T. Lindley

F. THE GUNN EFFECT IN n-CdTe*

In this section we report the observation of Gunn effect oscillations in n-type CdTe[†] for samples between 25 and 400 μ long prepared from crystals with low-field carrier concentrations between 5×10^{14} and $5.3 \times 10^{15} \text{ cm}^{-3}$. For samples longer than about 80 μ, the current oscillation is seen as a series of spikes separated by valleys with the period of oscillation increasing linearly with sample length.

The samples were prepared from polycrystalline n-type cadmium telluride crystals cut from ingots grown by a sealed ingot zone refining technique.¹⁶ Slices 0.020-inch thick were lapped and

* This section is based on the following thesis written in partial fulfillment of the requirements for the degrees of Master of Science and Electrical Engineer: M. R. Oliver, "Negative Resistivity Effects in CdTe," Department of Electrical Engineering, M.I.T., 19 January 1967.

† The crystals of CdTe were supplied by Dr. G. W. Ludwig and the late Dr. R. E. Halsted of the General Electric Research and Development Laboratory.

finally polished in an etch of bromine and methanol. Samples were then made from the polished slice by cleaving. Contacts were alloyed to each sample by pressing 0.020-inch indium dots against two opposite sides of the sample until they stuck, and then heating the sample to about 300°C for a few seconds in a reducing atmosphere of forming gas (85 percent Ar, 15 percent H₂) and HCl. Each sample was mounted in a tunnel diode package for testing. If the sample was ohmic with about the correct low-field resistance, as calculated from the bulk properties of the crystal, the high electric field properties were examined. Typical sample dimensions were $400 \times 400 \mu$ with a thickness ranging from 25 to 450 μ .

The current and voltage waveforms for these samples were measured under pulsed operation to avoid heating. The pulse lengths ranged from 3 to 50 nsec at repetition rates of 50 to 150 per second. The pulse forming network consists of a pulse generator which discharges a coaxial delay line through a mercury-wetted relay. The samples were evaluated in a resistive network so that the sample waveforms would not be modified by resonant circuit effects. The evaluation circuit is shown in Fig. I-15.

The current-voltage characteristic for a typical sample is shown in Fig. I-16. As may be seen, the sample is ohmic at low voltages, with the current showing a tendency to saturate as the voltage is increased. Above a threshold voltage, the current oscillates in time, and the average current drops. After several oscillations, however, there is a small increase observed in the sample current. As the driving voltage is increased further, this current increase becomes larger and starts to occur nearer the beginning of the pulse. For sufficiently large driving voltages (or for long pulses), the current increase becomes large and the sample voltage drops below the Gunn effect threshold. In this high current state, the current waveform (as observed on a sampling oscilloscope), does not appear to have any repetitive Gunn effect oscillations.

In the driving voltage region for which Gunn effect oscillations are seen, the current waveform usually took the form of repetitive oscillations. In Fig. I-17, we see a typical current waveform for a 150- μ long sample from a crystal with $n = 5 \times 10^{14} \text{ cm}^{-3}$ and $\mu = 1100 \text{ cm}^2/\text{V sec}$. The current follows the pulse voltage to the Gunn effect threshold, then oscillates in time within a range of current, and then increases as the pulse continues, finally switching to a high current state with the sample voltage decreasing below the Gunn effect threshold. The current increase, and subsequent switching to a high conductance state will be discussed in the next section.

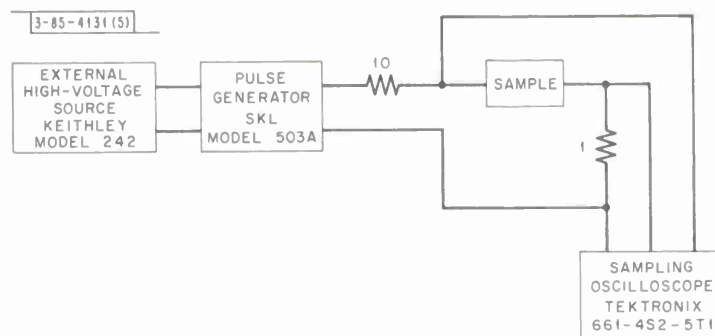


Fig. I-15. Circuit used to measure sample current and voltage as a function of time.

-85-6009

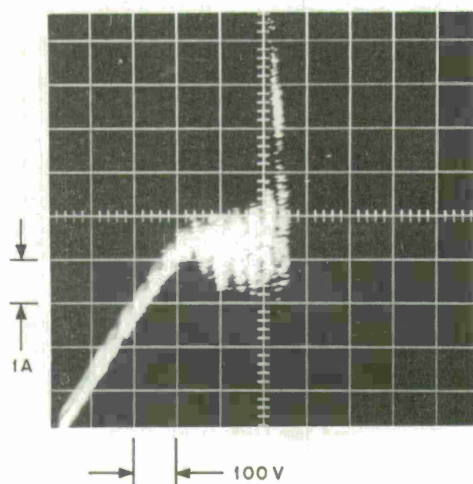


Fig. I-16. Current-voltage characteristic for a 380- μ long sample of n-CdTe with room temperature carrier concentration of $1.2 \times 10^{15} \text{ cm}^{-3}$.

-85-6010

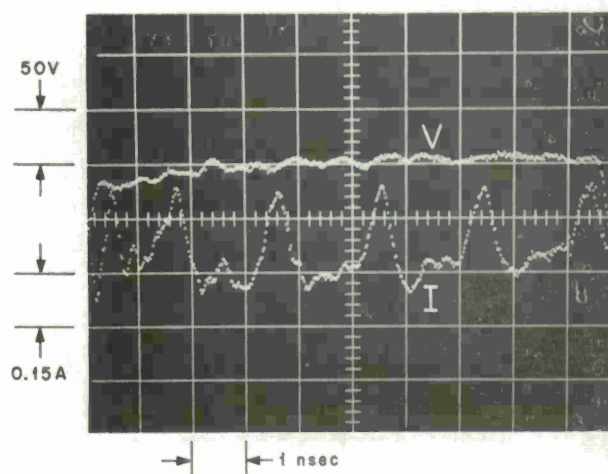


Fig. I-17. Current and voltage waveforms for a 175- μ sample of n-CdTe with room temperature carrier concentration of $5 \times 10^{14} \text{ cm}^{-3}$.

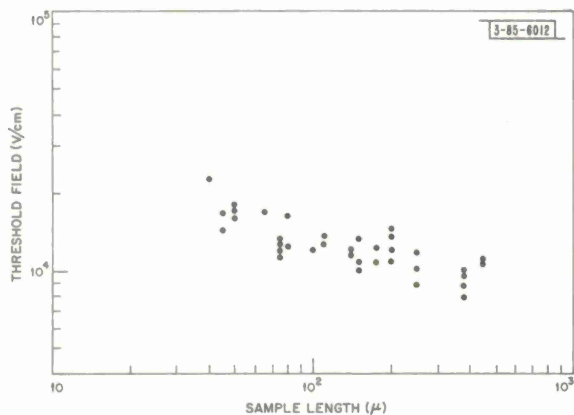


Fig. I-18. Threshold electric field vs sample length for n-CdTe at $T = 300^\circ \text{K}$.

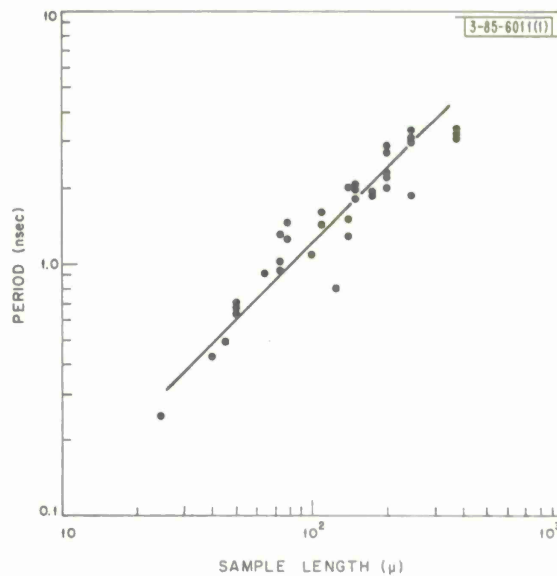


Fig. I-19. Oscillation period vs sample length for n-CdTe at $T = 300^\circ \text{K}$.

The threshold electric field (defined as the threshold voltage divided by the sample length) for Gunn effect oscillations is shown in Fig. I-18 for uniform cross section samples of various lengths. As may be seen, the threshold electric field decreases slowly with increasing sample length. On the other hand, the threshold values of electron drift velocity (defined as the threshold current density divided by $n_0 e$, where n_0 is the equilibrium carrier concentration) appeared to be independent of sample length with a value of about 1.3×10^7 cm/sec.

For samples longer than about 80μ , the current oscillation is seen as a train of more or less well defined spikes (as shown in Fig. I-17). The period of these spike waveforms was linearly related to the sample length, as shown in Fig. I-19. From this figure, we may estimate the velocity of high field domains which cause the current oscillation to be about 0.7×10^7 cm/sec, approximately one-half the threshold electron drift velocity.

Several samples were cooled to 77°K , to observe their Gunn effect behavior at low temperatures. The threshold electric field at this temperature dropped to about 8,000 V/cm, and the transit time of domains decreased by about 25 percent. The current swing appeared larger at 77°K , and the sample current ran away much more easily.

M. R. Oliver
A. G. Foyt

G. CURRENT RUNAWAY AND AVALANCHE EFFECTS IN n-CdTe

We have observed effects in n-CdTe which indicate that in addition to the Gunn oscillations already reported,¹⁷ there is a current runaway caused by a bulk avalanche of hole-electron pairs. In this section we wish to discuss the experiments, particularly the observation of light-emitting filaments reaching from one contact of the sample to the other contact, which have led to this interpretation.

The samples were prepared from crystals of n-CdTe* with room temperature mobilities of $\approx 1100 \text{ cm}^2/\text{V sec}$ and carrier concentrations between 5×10^{14} and $5 \times 10^{15} \text{ cm}^{-3}$. Sample cross sections were typically $400 \times 400 \mu$ with thickness ranging between 25 and 450μ . Each sample was placed in a resistive circuit¹⁷ and biased on a pulse basis, usually with 10 to 20 nsec pulses at a repetition rate of 100 sec^{-1} .

The important characteristics of the runaway can be seen in the sequence of current and voltage traces in Fig. I-20. The results for three different voltage drives to the circuit are shown, with voltage increasing from (a) to (c). As may be seen, the runaway is preceded by a small increase in the DC current level during the Gunn oscillations. This current runaway, observed in all the samples tested, was found to occur sooner in the pulse as the driving voltage was increased above the Gunn effect threshold. The sustaining voltage for each sample was always about 10 percent below the Gunn threshold ($\sim 10,500 \text{ V/cm}$).

As an initial diagnostic experiment, we used a photomultiplier with an S-1 photosensitive surface to look for infrared radiation from the sample during Gunn oscillations and runaway. No light was detected until the current started to run away, after which the intensity of emitted light followed the current increase. The wavelength of the emitted radiation was about 8600 \AA

* The crystals were kindly supplied by Dr. R. E. Halsted of the General Electric Research and Development Laboratory, Schenectady, N.Y.

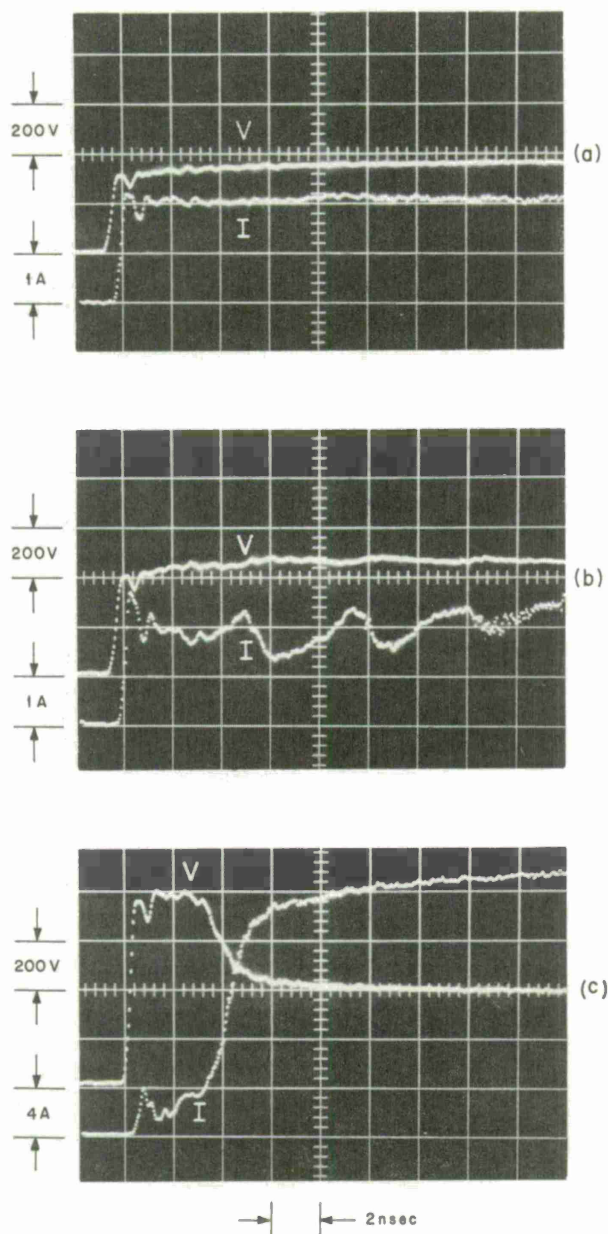


Fig. I-20. Current and voltage waveforms illustrating the current runaway for a $380\text{-}\mu$ long sample of n-CdTe with room temperature carrier concentration of $1.2 \times 10^{15} \text{ cm}^{-3}$. (a) Voltage below Gunn threshold; (b) voltage above Gunn threshold, with current exhibiting several oscillations before beginning runaway; (c) voltage starting well above Gunn threshold, with current increasing (and voltage decreasing) rapidly after about one Gunn oscillation; note scale change on current.

(with a half-power width of 300 \AA), approximately the bandgap energy in CdTe, indicating the presence of excess holes in the sample.

In order to spatially resolve the emitted radiation, the edge of the sample was examined through a microscope and an infrared image converter. The light was observed to be emitted from filaments, reaching from one contact to the other. These filaments appeared to be uniformly bright throughout their length and moved about the sample with time. The filaments grew and faded in intensity, giving the impression that they were moving toward and away from the observed sample edge. The total emitted radiation produced after a 3 nsec voltage pulse* was at least 10 percent of that expected if all the conductivity change were due to excess hole-electron pairs and if all these pairs recombined radiatively.

The above set of results suggests a current-controlled bulk differential negative resistivity produced by the generation or injection of hole-electron pairs in the sample. As Ridley¹⁸ has shown, such a negative resistivity will lead to a current increase, filament formation, and a decrease in voltage across the sample if the sample is biased above a critical value.

We have considered three mechanisms in order to explain the presence of excess holes in the samples: (1) injection of holes from a contact, (2) generation of hole-electron pairs in the high-field region of traveling domains associated with the Gunn effect oscillations, and (3) low-field avalanche near the Gunn effect threshold, a model originally proposed by Copeland¹⁹ for n-GaAs. The first mechanism was eliminated by observing that the current runaway and the uniformly bright filament formation took place in a $150\text{-}\mu$ long sample biased with a 3-nsec voltage pulse, whereas holes injected from a contact would have been able to drift only a small fraction of the sample length during this time.

The second mechanism, generation in a high-field domain, was proposed by Southgate, *et al.*,²⁰ as an explanation for the current runaway and infrared light emission seen in heavily doped n-GaAs. It would appear to be operative in n-CdTe also, as we have not observed current runaway without first seeing some evidence of Gunn oscillations. However, once the runaway has been started, the sustaining voltage drops below the Gunn effect threshold, and the current waveform, as seen on a sampling oscilloscope, shows no repetitive Gunn effect oscillations. The light output, on the other hand, continues to follow the current increase, even though Gunn oscillations are no longer observed.

We were therefore led to consider whether the current runaway could be sustained by low-field avalanche,[†] with the generation of a critical density of hole-electron pairs the only role of the high-field domains. In order to test this idea, we tried to generate the hole-electron pairs by using penetrating light from a GaAs laser operated at 77°K . Although the sample conductivity could be doubled by the laser, an increase comparable to that at the beginning of normal runaway, it was never possible to produce runaway without some Gunn oscillations first occurring. However, as the light intensity was increased, the runaway did occur nearer the beginning of the pulse for a fixed voltage drive, or at a lower voltage for a fixed time lag. These results

* Negligible recombination radiation should have occurred during the pulse. By the use of a two-level voltage pulse, the conductivity decay time was found to be between 20 and 40 nsec in agreement with the low-field photoconductivity relaxation time of about 50 nsec measured using a GaAs laser as a light source.

† Low-field avalanche of the type proposed by Copeland¹⁹ should be much more probable in CdTe than in GaAs since in CdTe the energy separation between the subsidiary conduction band minima and the $k = 0$ minimum appears to be nearly equal to the bandgap.²¹

Section I

are somewhat ambiguous because of the uncertainty of the critical density of hole-electron pairs needed, but seem to indicate that the high-field domains play a more complex role than hypothesized above. Unfortunately, the question of the low-field avalanche remains unanswered.

In conclusion, the current runaway effects observed in these experiments are consistent with a bulk current-density controlled differential negative resistivity caused by a bulk avalanche of hole-electron pairs. Although the avalanche is probably initiated by traveling high-field Gunn domains, the mechanism that sustains the current runaway is not understood.

M. R. Oliver
A. L. McWhorter
A. G. Foyt

REFERENCES

1. J. F. Butler, J. Electrochem. Soc. 111, 1150 (1964).
2. E. R. Washwell and K. F. Cuff, in Radiative Recombination in Semiconductors (Dunod, Paris, 1964), p. 11.
3. Solid State Research Report, Lincoln Laboratory, M.I.T. (1967:2), p. 6, DDC 656548.
4. C. E. Hurwitz, Appl. Phys. Letters 8, 121 (1966).
5. ———, Appl. Phys. Letters 9, 420 (1966).
6. E. J. Sternglass, Phys. Rev. 95, 345 (1950).
7. J. E. Holliday and E. J. Sternglass, J. Appl. Phys. 28, 1189 (1957).
8. L. Holland, Vacuum Deposition of Thin Films (Wiley, New York, 1958), p. 322.
9. D. C. Reynolds, C. W. Litton and T. C. Collins, Phys. Rev. 156, 881 (1967).
10. P. J. Dean, J. D. Cuthbert, D. G. Thomas, and R. T. Lynch, Phys. Rev. Letters 18, 122 (1967).
11. A. G. Foyt and C. M. Wolfe, Proceedings of the International Symposium on Gallium Arsenide, Reading, 1966 (Institute of Physics and the Physical Society, London, 1967), p. 181; Solid State Research Report, Lincoln Laboratory, M.I.T. (1966:4), p. 11.
12. L. J. van der Pauw, Philips Res. Rep. 13, 1 (1958).
13. A. H. Wilson, The Theory of Metals (Cambridge University Press, London, 1954), p. 236.
14. C. O. Thomas, O. Kahng and R. C. Manz, J. Electrochem. Soc. 109, 1055 (1962).
15. I. Amron, Electrochem. Tech. 5, 94 (1967).
16. M. R. Lorenz and R. E. Halsted, J. Electrochem. Soc. 110, 343 (1963); B. Segall, M. R. Lorenz, and R. E. Halsted, Phys. Rev. 129, 2471 (1963).
17. A. G. Foyt and A. L. McWhorter, IEEE Trans. Electr. Dev. ED-13, 79 (1966).
18. B. K. Ridley, Proc. Phys. Soc. 82, 954 (1963).
19. J. A. Copeland, Appl. Phys. Letters 9, 140 (1966).
20. P. D. Southgate, H. J. Prager and K. K. N. Chang, to be published in J. Appl. Phys.
21. J. L. Shay, W. E. Spicer and F. Herman, Phys. Rev. Letters 18, 649 (1967).

II. OPTICAL TECHNIQUES AND DEVICES

A. STABILITY MEASUREMENTS OF CO₂-N₂-He LASERS AT 10.6 μ m WAVELENGTH

Measurements of the short-term stability¹ of the beat frequency²⁻⁴ of two stable, single frequency (TEM_{00q} mode) CO₂-N₂-He lasers has been continued. Both lasers were sealed-off and free-running without any feedback stabilization. The width of the spurious frequency modulation was typically less than 10 kHz for observation times of several seconds and less than 1 kHz for tens of milliseconds. The slow drift rate of the beat frequency often did not exceed a few hundred Hz/sec for several minutes. These results constitute at least a factor of 10 improvement over the typical figures described previously.^{5,6} The observed frequency jitter was caused by environmental fluctuations such as acoustic vibrations, plasma instabilities, power supply noise, variations of temperature and pressure, etc. Therefore, these measurements should not be confused with the ultimate spectral width of a laser oscillator as determined by quantum noise.³

Figure II-1 shows one of the DC-excited internal mirror tubes used in these experiments. Two massive 6-in. square stainless steel mirror holders are rigidly held apart by four 1-in. diameter invar rods. The mirrors are seated in the reentrant portion of the stainless steel holders; this design feature provides at least partial compensation against changes in the optical cavity length due to temperature variation. The water cooled discharge tube section was operated with a 20-cm long gas discharge in the optical cavity. The optical cavity and the differential screw tuning mechanism added to one of the mirror holders was described previously.⁵

During the stability measurements the lasers were acoustically isolated in an audiometric booth lined with fiberglass. This booth weighed nearly 2000 lb, and was isolated from floor vibrations by inflated rubber shock mounts. After careful alignment, the two laser beams were recombined by a dielectrically coated Irtran beam-splitter. The recombined beam was detected by a liquid-nitrogen-cooled gold-doped germanium detector which was externally loaded by 1 k Ω , or by 93 Ω . The detector and the amplifier following it limited the observation of beat frequencies to less than 30 MHz.

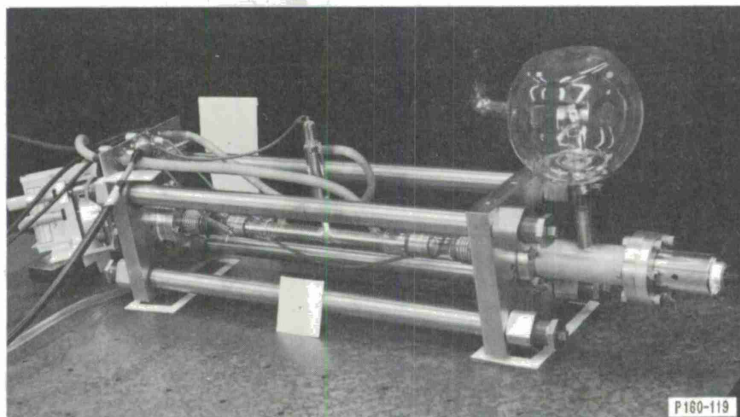
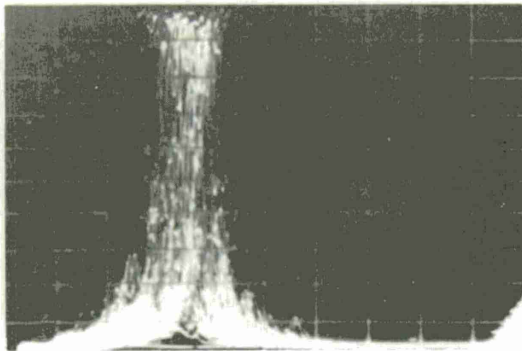
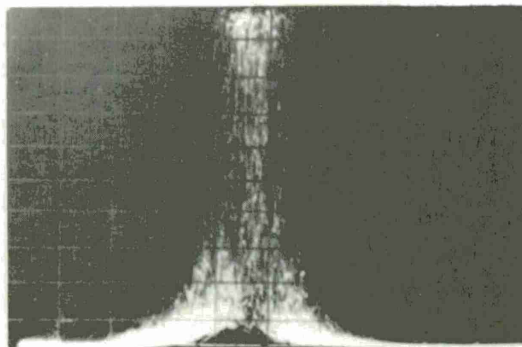


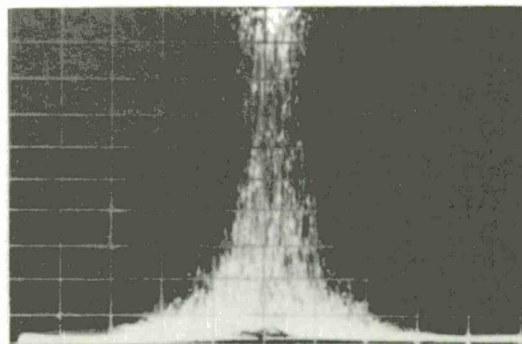
Fig. II-1. Stable, single frequency, sealed-off CO₂-N₂-He laser.



(a)

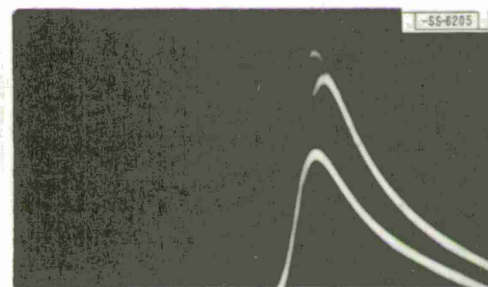


(b)

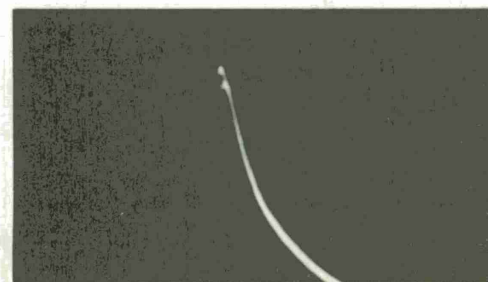


(c)

Fig. II-2. Spectrum analyzer display of beat frequency: vertical scale linear; IF bandwidth 5 kHz; horizontal dispersion 10 kHz/cm; sweep rate 60 Hz/sec; exposure time (a) 1 sec. (b) 2 sec. (c) 4 sec.



(a)



(b)

Fig. II-3. Spectrum analyzer display of beat frequency: vertical scale linear; IF bandwidth 1 kHz; horizontal dispersion 10 kHz/cm; sweep rate (a) 10^{-2} sec/cm, (b) 5×10^{-3} sec/cm; exposure time (a) 2.5×10^{-1} sec, (b) 1.25×10^{-1} sec.

The beat frequency was tunable from essentially zero to about 30 MHz, and spectrum analyzer displays similar to Fig. II-2 were produced. One-, two-, and four-second film exposure times were used to photograph Figs. II-2(a), 2(b) and 2(c), respectively. This figure shows that the envelope for the combined frequency drift and jitter contributed by both lasers was typically less than 6 to 10 kHz for observation times of several seconds. Measurements with a stop watch also indicated that the drift rate of the beat frequency often did not exceed a few hundred Hz/sec for several minutes.

The display shown in Fig. II-3(a) is indicative of the amount of stability for a time duration of 100 msec. The 10-msec/cm sweep rate and the 250-msec exposure time of the camera allowed the integration of two or three consecutive analyzer sweeps on the photograph. The peaks of the frequency spikes are less than 2 kHz apart on Fig. II-3(a). The IF bandwidth of the spectrum analyzer was set to 1 kHz for Fig. II-3(a) and 3(b). Figure II-3(b) was photographed with a 125-msec film exposure time and a 5-msec/cm sweep rate of the analyzer. The resulting two frequency spikes are almost overlapping and thus indicate a frequency stability of less than 1 kHz for a time duration of 50-msec. A 50-msec time duration corresponds to a radar round trip return from an object approximately 7,500 km away. Using the effective spectrum analyzer resolutions shown in Fig. II-3, single scan displays of the beat frequency often could not be distinguished from those produced by a high quality Hewlett Packard signal generator.

The measurements described here are considered only preliminary. Their purpose is to test some of the design features of the lasers and to facilitate choosing from among the different approaches pertaining to more refined frequency stability measurements as partially outlined in the February 1966 IEEE Proceedings.¹

C. Freed

B. CONTINUOUS OPERATION OF A LONG-LIVED SEALED CO₂ LASER TUBE. EFFICIENCY OF A SEALED CO₂ LASER TUBE

The work reported on in the last Solid State Research Report⁷ has been continued to determine the conditions for operating a sealed CO₂ laser tube continuously. This would infer no absorption of the gases at the cathode. The tube operation discussed previously was interrupted periodically to regenerate the CO₂ in an almost completely reversible reaction at the cathode after gas absorption had taken place during the discharge. The tube with associated equipment was similar to the experimental set up reported on previously, except that both electrodes were of pure nickel, were not water cooled, and the cathode envelope was heated continuously, at a temperature of 300°C.

The discharge in the CO₂, N₂, He mixture of the tube reported on in the previous quarter⁷ produced large concentrations of CO and O₂ which reacted with the Ni cathode forming compounds that probably included NiO and carbonate, CO₃⁼, complexes. The formation of these deposits at the cathode by reactions with O₂ and CO soon (initially 335 hours) exhausted the supply of CO₂ within the tube. Then by extinguishing the discharge, the CO₂ was released back into the tube by heating the cathode and breaking down the carbonates. It is desirable to prohibit chemical sputtering and compound formation at the cathode or reverse these processes continuously during tube operation so that stopping periodically to regenerate CO₂ would not be necessary. Maintaining the cathode envelope at 300°C accomplished this continuous operation for more than 1000 hours of operation and the tube is still running. At this time there is a pronounced absence of

Section II

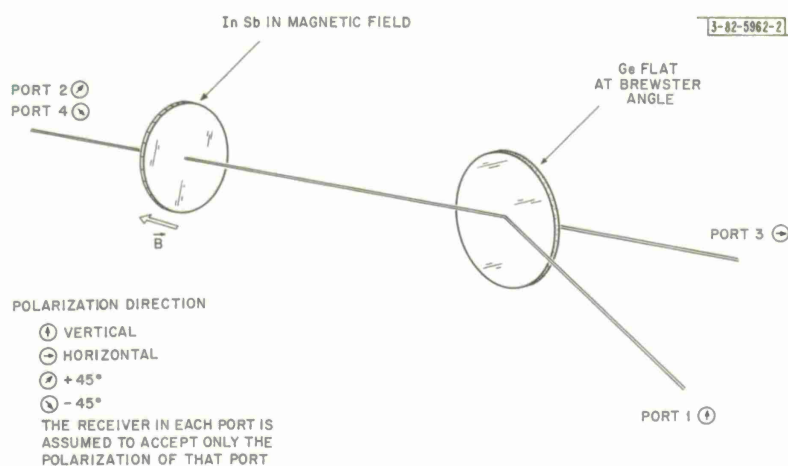


Fig. II-4. A 10.6- μ four-port circulator.

3-82-5982 (1)

INPUT	OUTPUT			
	1	2	3	4
1	<0.001	0.7 [†]	<0.001	<0.001*
2	<0.001	<0.001*	0.9 [†]	<0.001*
3	<0.001	<0.001*	<0.001*	0.9 [†]
4	0.7 [†]	<0.001*	<0.001 [‡]	<0.001*

* Values marked with an asterisk are estimated; others are measured.

[†] 55 percent reflection loss in InSb is disregarded because it could be eliminated with anti-reflection coatings.

[‡] 0.18 of port 4 signal, vertically polarized, will leak into the direction of port 3.

Fig. II-5. Matrix of 10.6- μ circulator.

sputtered material and no evidence of chemical action at the electrodes. The power output at $10.6\ \mu\text{m}$, the tube pressure, and the discharge electrical characteristics have changed only about 2 percent over this time interval. A considerable change in the side radiation took place at approximately 800 hours of operation and is probably due to an increase in hydrogen in the tube which also accounts for the slight pressure increase. This hydrogen increase was measured in the tube discussed in the last report, and similar changes in side radiation occurred.

The output power at $10.6\ \mu$ has fluctuated during the 800 hours of operation. This power variation has been definitely attributed to the salt Brewster windows eroding in a humid atmosphere. Each time a large drop in power occurred the windows were repolished in place and the output power was substantially restored, as for example, at 800 hours the output was 5.1 W. Initially the power output was 6 W.

The efficiency of a sealed-off CO_2 laser was checked using an internal mirror pyrex laser tube with a 25-mm bore and 126-cm discharge length in a 154-cm cavity. The tube was filled with 3 torrs of CO_2 , 3 torrs of N_2 , and 6 torrs of He.

When discharged using Ni electrodes with a current of 25 mA, a multimode output of 42 W was achieved at $10.6\ \mu$ through a 22 percent transmission mirror with a resulting efficiency of 12 percent. This efficiency is a factor of about two greater than previously measured for single mode Brewster window tubes and approaches the efficiency of CO_2 flowing gas systems.

R. J. Carbone

C. INFRARED HETERODYNE DETECTION

Heterodyne experiments have been performed in the middle infrared region of the electromagnetic spectrum using the CO_2 laser as a radiation source. Detectors of photovoltaic $\text{Pb}_{1-x}\text{Sn}_x\text{Se}$, operated at 77°K, have achieved theoretically optimum operation for kHz and MHz heterodyne frequencies. In accordance with the theory, the minimum detectable power observed is a factor $2/\eta$ greater than the theoretically perfect quantum counter, $h\nu\Delta f$. The coefficient $2/\eta$ has a value 25 for the $\text{Pb}_{0.936}\text{Sn}_{0.064}\text{Se}$ detector used in this study.

Further improvements in heterodyne sensitivity may be expected since the quantum efficiency of detectors such as $\text{Pb}_{1-x}\text{Sn}_x\text{Se}$ and $\text{Pb}_{1-x}\text{Sn}_x\text{Te}$, which is presently ≈ 8 to 15 percent, shows promise of being even greater in the future.

M. C. Teich

D. A 10.6-MICRON FOUR-PORT CIRCULATOR USING FREE CARRIER ROTATION IN InSb

Free carrier Faraday rotation in InSb^8 has been used to make a low loss four-port circulator for $10.6\text{-}\mu$ radiation as shown in Fig. II-4. Thirty-db isolation (1000:1 in power) has been achieved between ports 2 and 1, and 1 and 3. The device may be used to isolate a $10.6\text{-}\mu$ radar receiver (port 3) from its transmitter (port 1), with transmitted radiation emerging from port 2, or to isolate a master oscillator (port 1) from a power amplifier or oscillator (port 2) which it controls. A germanium plate of Brewster's angle was used as a polarizer. It does not have all the features of a perfect polarizer, hence the matrix elements of the circulator as shown in Fig. II-5 are not ideal. In determining the matrix element, the receiver in each port is assumed sensitive only to the polarization of that port. Power from port 4 will leak in the direction of port 3 but will be vertically polarized. Also, power from port 2 is in the same

Section II

direction as port 4 but is polarized at right angles. The reflection from the InSb does not affect the matrix elements because tilting the InSb slightly will cause the very narrow reflected beam to be lost, its only effect on the elements being from scattering.

The 0.5-mm thick InSb sample has a carrier concentration of $2 \times 10^{17} \text{ cm}^{-3}$, a mobility of $45,000 \text{ cm}^2/\text{volt sec}$, and absorbs 10 percent of the beam. It also has a reflection loss of 55 percent, because antireflection coatings were not used in this preliminary experiment. Forty-five degree rotation was achieved with a field of 5300 gauss. The 0.5-cm diameter CO_2 beam was passed through a 0.6-cm hole drilled in the pole pieces of a 6-in. Varian magnet. The gap (2.5 cm) was sufficient to preserve a field uniformity of 1 percent midway between the pole pieces. Thirty-db isolation was achieved with this arrangement.

There are three other properties of the material which must be considered in optimizing the design of this device. One is the interband Faraday effect which sets a minimum on the electron concentration that can be used. The interband Faraday rotation is equal and oppositely directed to the free electron Faraday effect at a carrier concentration of about 10^{15} cm^{-3} . In order for the free electron effect to dominate the interband effect the carrier concentration must be about $4 \times 10^{16} \text{ cm}^{-3}$.

Another phenomena⁹ which must be considered is the very large absorption cross section of holes, which is about 40 times that of electrons at 10.6μ . At room temperature $n_i^2(T)$ is about $2 \times 10^{32} \text{ cm}^{-6}$. If there are $4 \times 10^{16} \text{ cm}^{-3}$ electrons, there will be 0.5×10^{16} holes which means that the absorption due to holes will be five times that of electrons, making this carrier concentration unsuitable for room temperature operation when high powers are to be controlled.

The third property is the thermal conductivity^{10,11} of the material which will limit the power handling capability of the device, either through thermal runaway or optical distortion unless a means is provided to conduct heat away from the surface of the InSb disc.

If the electron concentration is high enough and the temperature low enough so that the ratio of the number of electrons to the number of holes is much greater than 40, then the ratio of Faraday rotation to absorption is equal to $1/2 \mu\text{B}$. The mobility¹² decreases as the carrier concentration increases, so that using a higher carrier concentration than necessary to make the hole concentration small, or to override the interband effect, is not advisable. For room temperature operation a sample about 0.025-cm thick with an electron concentration of $4 \times 10^{17} \text{ cm}^{-3}$ would work in a moderate magnetic field (5000 gauss). It would have to be thermally bonded to something with good thermal conductivity and transmission at 10.6μ such as germanium, by a method that preserves optical transmission at that wavelength, if high powers are to be controlled. An alternative method might be to blow a gas stream over it, but care must be taken to preserve the interferometric quality at the optical path.

If operation at liquid nitrogen temperatures is admissible, then the thicker sample of $4 \times 10^{16} \text{ cm}^{-3}$ electron concentration would handle 100 W without any elaborate bonding scheme, since the thermal conductivity is six times higher than at room temperature.

Work is in progress to determine the power handling capability experimentally.

Jane H. Dennis

REFERENCES

1. Proc. IEEE 54, February (1966), Special Issue on Frequency Stability.
2. T.S. Jaseja, A. Javan, and C.H. Townes, Phys. Rev. Letters 10, 165 (1963).
3. A.E. Siegman, B. Daino, and K.R. Manes, "Preliminary Measurements of Laser Short-Term Frequency Fluctuations," IEEE J. Quant. Electron. QE-3, 180 (1967).
4. R.A. Brandewie, W.T. Haswell III, and R.H. Harada, IEEE J. Quant. Electron. QE-2, 756 (1966).
5. Solid State Research Report, Lincoln Laboratory, M.I.T. (1967:1), DDC 651065.
6. C. Freed, IEEE J. Quant. Electron. QE-5, 203 (1967).
7. Solid State Research Report, Lincoln Laboratory, M.I.T. (1967:2), p.16, DDC 656548.
8. S.D. Smith, T.S. Moss and K.W. Taylor, "The Energy Dependence of Electron Mass in Indium Antimonide Determined from Measurements of the Infrared Faraday Effect," J. Phys. Chem. Solids 11, 131 (1959).
9. S.W. Kurnick and John M. Powell, "Optical Absorption in Pure Single Crystal InSb at 298° and 78°K," Phys. Rev. 116, 597 (1959).
10. Audrey D. Stuckes, "Thermal Conductivity of Indium Antimonide," Phys. Rev. 107, 427 (1957).
11. C. Hilsum, R.K. Willardson and A.C. Beer, Semiconductors and Semimetals, Vol. 2 (Academic Press, New York, 1966), p.13.
12. C. Hilsum and A.C. Ross-Innes, Semiconducting III-V Compounds (Pergamon Press Inc., New York, 1961), p.128.

III. MATERIALS RESEARCH

A. MEASUREMENT OF TRACE OXYGEN AND WATER VAPOR IN INERT GASES

Most high temperature chemical systems are particularly sensitive to oxygen or water vapor, even at concentrations well below 1 ppm. The inert gases argon and helium are frequently used as protective atmospheres for such systems, including many of those employed in the growth of single crystals at high temperatures. Commercial cylinders of these gases usually contain 5 to 50 ppm available oxygen (O_2 and H_2O). By using a hot refractory metal getter such as titanium, the available oxygen content can be reduced to 10^{-8} ppm, giving an available oxygen partial pressure of 10^{-11} torr.¹ However, the purified gas is often unwittingly contaminated in handling, and available oxygen concentrations as high as 100 ppm may easily be reached at the location where the gas is used. For this reason it is important to monitor the available oxygen content. A simple method has been developed for this purpose.

In the new method, a measurement is made of the increase in resistance of a tightly coiled tungsten filament due to oxidation by measuring the current through the filament at constant applied voltage. The currents used are high enough to heat the filament to 1700 – 1850°K, a temperature range in which tungsten oxide is volatile. It has been found that over a wide range of operating conditions the rate of decrease in current is initially constant, and that this initial rate is proportional to available oxygen content up to at least 200 ppm.

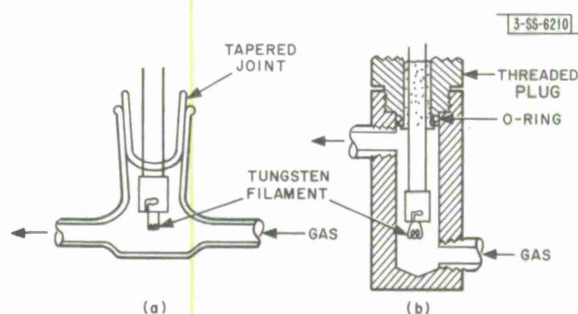


Fig. III-1. Test cells for measuring available oxygen content of inert gases. (a) Glass; (b) metal.

The tungsten filament is obtained from a No. 47 incandescent light bulb by breaking the glass envelope. Two types of cells have been used for mounting the filament in the gas stream. The glass cell shown in Fig. III-1(a) is used with glass gas-handling systems, and the metal cell shown in Fig. III-1(b) is used with all-metal systems.

The measured dependence of current on time for a coiled filament operated at 6.3 V in argon containing 60 ppm O_2 is shown in Fig. III-2, together with data obtained under the same conditions for a straight filament obtained by stretching out a coiled filament. For the coiled filament, the current decreases at a constant rate to about one-half its initial value, then decreases more and more rapidly until the filament burns out. For the straight filament, the rate of current decrease remains constant only until the current reaches about 90 percent of its initial value. Therefore a straight filament is much less convenient to use for oxygen measurements than a coiled one.

It was observed that the initial rate of current change for a coiled filament was independent of gas flow rate between 85 and 1000 cm^3/min , and also that it was the same in both glass and metal cells. A plausible explanation of these observations is that at fixed oxygen content the

Section III

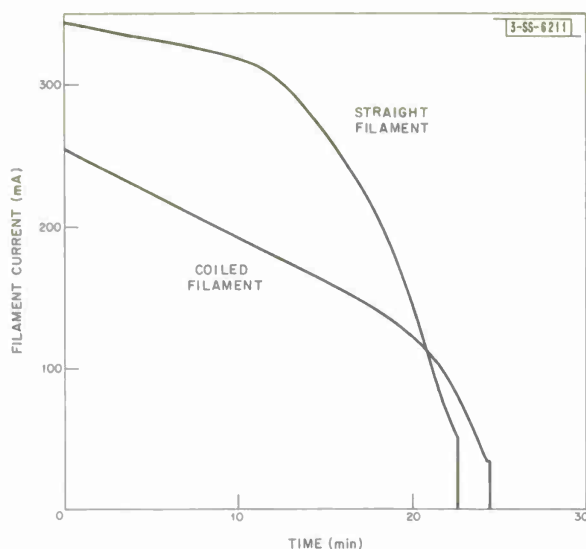


Fig. III-2. Current vs time for coiled and straight tungsten filaments operated at 6.3 V in argon containing 60 ppm O_2 .

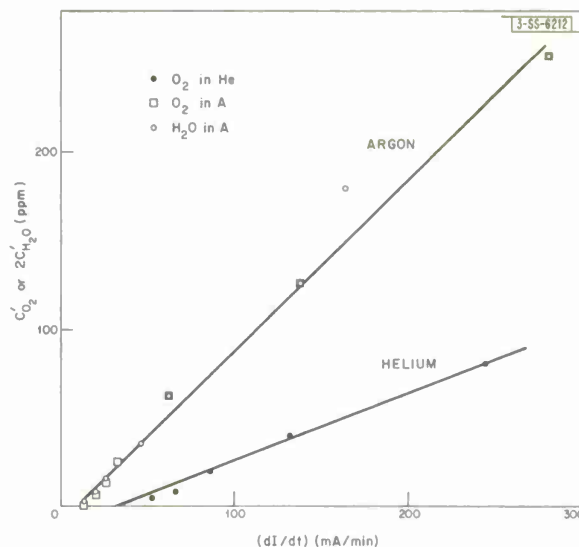


Fig. III-3. Initial rate of current change as a function of available oxygen content for coiled tungsten filaments operated in argon or helium mixed with O_2 or water vapor.

oxidation rate depends primarily on the rate of natural convection around the filament, and that this rate is initially constant because the coil radius remains constant even though the wire radius is decreasing due to oxidation.

To calibrate the cells for measuring available oxygen, the initial rate of current change for a coiled filament (dI/dt) was determined for gas streams produced by mixing cylinder argon or helium with known amounts of oxygen or water vapor. The results are shown in Fig. III-3, where the concentrations of added oxygen (C'_{O_2}) and water vapor ($2C'_{H_2O}$) are plotted against (dI/dt) . Since the finite rate of oxidation at $C' = 0$ can be attributed to the presence of about 10 ppm of available oxygen in the cylinder gases, the data are well represented by the equation $C_{O_2} = k(dI/dt)$, where C_{O_2} is the total concentration of available oxygen and k is a cell constant which depends on the gas used. The operating conditions used and the values of k derived from the data are given in Table III-1. As expected, water vapor is half as effective as the same concentration of oxygen in oxidizing the filament.

After calibration, the glass cell was used to measure C_{O_2} in helium and argon under a variety of experimental conditions. The results are summarized in Table III-2. They show that polyvinyl chloride tubing is a source of serious contamination, even after prolonged purging. It was also found that copper tubing must be flamed or purged to avoid introducing oxygen at the ppm level. When properly treated copper tubing was used, the value of C_{O_2} in titanium-gettered argon after 2 days of purging was reduced to less than 0.02 ppm, the lowest concentration which caused a detectable change in filament current in 6 h of operation. When gas of this purity was used as the protective atmosphere in a resistance furnace operated above 2000°C, the life of the tantalum

TABLE III-1 CELL CONSTANTS FOR MEASURING AVAILABLE OXYGEN CONTENT OF ARGON AND HELIUM					
Gas	Flow rate (cm ³ /min)	T°K	Voltage (V)	I _o (mA)	k (ppm/mA/min)
Argon	400	1700	6.3	450	9.6
Helium	1250	1820	12.0	240	3.3

TABLE III-2 AVAILABLE OXYGEN CONTENT OF ARGON AND HELIUM UNDER VARIOUS EXPERIMENTAL CONDITIONS				
Gas	Tubing	Treatment	Purging Time (h)	C _{O₂} (ppm)
Helium	Polyvinyl chloride (3 m)	As received	(Initial)	68
	Polyvinyl chloride (3 m)	As received	40	39
	Copper	As received	48	10
	Copper	Saturated with water vapor at 0°C	(Initial)	400
Argon	Copper	As received	48	23
	Copper	Titanium-gettered	24	0.3
	Copper	Titanium-gettered	48	<0.02

Section III

elements was extended by a factor of 10, although the consumption of argon had been reduced by a factor of 4.

T. B. Reed
W. J. LaFleur

B. GROWTH OF CrBr_3 SINGLE CRYSTALS

Single crystals of CrBr_3 up to about 10 mm on a side have been grown by sublimation of the compound in sealed silica ampoules. Attempts to use the vapor transport method of Tsubokawa² were unsuccessful, yielding only small platelets rather than massive crystals.

To prepare CrBr_3 , argon was first bubbled through liquid bromine to saturate it with Br_2 vapor at room temperature, then passed over finely divided Cr powder heated to 650 °C. This procedure is similar to the one described by Brauer.³ A charge of CrBr_3 produced in this manner was placed at one end of a 20-mm inside diameter silica ampoule 90 mm long, the other end of which was tapered to a point. The ampoule was evacuated, sealed, and placed in a vertical resistance furnace with the tapered end at the top. The furnace was slowly heated to 900 °C. After the ampoule had been at this temperature for 24 h, it was pulled up out of the furnace at the rate of 9/16 in./day while being rotated at 6 rev/min. As the tapered end of the ampoule became cooler, CrBr_3 vapor condensed there to form a cone-shaped boule 20 to 25 mm long, which contained two to five single crystal grains.

A. Ferretti
E. J. Delaney

C. POLYMORPHISM IN Ag_2Te AT HIGH PRESSURES AND TEMPERATURES

The pressure-temperature diagram for Ag_2Te reported previously⁴ contains four phases: Ag_2Te -I, the monoclinic phase stable at room temperature and atmospheric pressure; a high-temperature f.c.c. phase which at atmospheric pressure is stable above 148 °C; and two high-pressure phases, Ag_2Te -II and Ag_2Te -III, which at room temperature are stable at 22 to 25 kbars and above 25 kbars, respectively.

Differential thermal analysis at hydrostatic pressures up to 14 kbars has been used to investigate the positions of the phase boundaries obtained earlier by means of resistivity measurements. Sharp deflections due to the transition from Ag_2Te -I to the f.c.c. phase were observed at temperatures reproducible to ± 1 °C. These transition temperatures are in good agreement with the earlier results.⁴ No detectible signals were obtained, however, on crossing the phase boundaries between Ag_2Te -I, Ag_2Te -II, and Ag_2Te -III.

In additional experiments with the Bassett high pressure x-ray camera,⁴ observations with a metallographic microscope were used in adjusting the pressure so that the entire area of the collimated x-ray beam was intercepted by Ag_2Te -II. Therefore a diffraction pattern due to this phase only has now been obtained. This pattern has been indexed on a tetragonal cell with $a = 8.92 \text{ \AA}$ and $c = 6.09 \text{ \AA}$, giving $c/a = 0.68$. The hkl value, d -spacing, and intensity for each diffraction line are given in Table III-3. The calculated density at pressure is 9.4 g/cm^3 , assuming eight molecules per unit cell. This corresponds to a density increase of 12 percent with respect to Ag_2Te -I at one atmosphere.

Comparison of the diffraction pattern for Ag_2Te -II with the pattern obtained earlier⁴ for Ag_2Te -III, which was indexed on a tetragonal cell, showed that the latter contains numerous lines

TABLE III-3
INDEXING OF X-RAY PATTERNS FOR
HIGH-PRESSURE $\text{Ag}_2\text{Te-II}$ AND $\text{Ag}_2\text{Te-III}$

$\text{Ag}_2\text{Te-II}$			$\text{Ag}_2\text{Te-III}$		
hkl	d-Spacing (Å)	Intensity	hkl	d-Spacing (Å)	Intensity
002	3.06	0.5	310,221	2.78	0.5
300	2.95	9	301,112	2.67	1
310	2.82	10	311	2.53	10
311	2.57	4	202	2.46	1
202	2.51	<0.5	400	2.17	8
321	2.31	1	410,302	2.11	8
400	2.25	1	411	1.99	<0.5
302,410	2.15	<0.5	322	1.90	0.5
330	2.10	<0.5	213	1.80	<0.5
411,003	2.04	8	402	1.76	<0.5
113	1.94	5	511	1.65	<0.5
402	1.80	0.5	521	1.56	0.5
510	1.75	<0.5	440	1.53	0.5
511	1.70	0.5	413	1.46	<0.5
313	1.65	<0.5	423	1.40	0.5
521	1.60	<0.5	324	1.29	0.5
530	1.53	1	424,115	1.20	0.5
610	1.47	2	524	1.10	<0.5
620	1.41	1			
541	1.36	1			
513	1.31	2			
700	1.28	1			
711,640	1.24	<0.5			
721	1.20	<0.5			
722	1.14	<0.5			
810	1.11	<0.5			

Section III

due to $\text{Ag}_2\text{Te-II}$. Therefore new measurements have been made with the Bassett camera at sufficiently high pressure to obtain a diffraction pattern due to $\text{Ag}_2\text{Te-III}$ only. This pattern has been indexed on a new tetragonal cell, with $a = 8.68 \text{ \AA}$, $c = 6.09 \text{ \AA}$, and $c/a = 0.70$. The hkl values, d -spacings, and intensities are listed in Table III-3. The calculated density at pressure is 9.9 g/cm^3 , assuming eight molecules per unit cell. This corresponds to a density increase of 18 percent with respect to $\text{Ag}_2\text{Te-I}$ at one atmosphere, and 5 percent with respect to $\text{Ag}_2\text{Te-II}$ at 25 kbars.

The space groups for $\text{Ag}_2\text{Te-II}$ and $\text{Ag}_2\text{Te-III}$ have not been determined. Although the two phases have the same c -parameter and similar a -parameters, they probably have different space groups, since the intensity distribution is quite different for the two diffraction patterns.

M. D. Banus
Mary C. Finn

D. CHARACTERIZATION AND STRUCTURE OF $\text{La}_4\text{Re}_6\text{O}_{19}$

When a lanthanum rhenium oxide with body centered cubic symmetry ($a \sim 9.0 \text{ \AA}$) was discovered⁵ several years ago, a single crystal x-ray study established that the space group was $I2_13$, $I23$, or $Im3$. However, the lack of sufficiently large single-phase samples prevented characterization and structure determination. A hydrothermal method has now been found for preparing such samples. A typical charge consisted of 2.0 g of La_2O_3 (99.999 percent), 4.2 g of ReO_3 , and 3 ml of water. The charge was placed in a 1/8-in. diameter gold tube about 5 in. long, which was sealed by welding at both ends. The tube was generally heated to 700°C for 12 h under an external pressure of 3000 atm. The reaction product was multiphase, but only crystals of $\text{La}_4\text{Re}_6\text{O}_{19}$ remained after washing with 6N HCl.

Chemical analysis for lanthanum with EDTA gave 28.0 percent, compared with 28.10 percent calculated. Thermogravimetric analysis in an H_2/Ar (15 percent) atmosphere showed that 10.5 percent of the sample was associated with reducible rhenium; a weight loss of 10.52 percent is calculated. The density of the crystals was determined by the standard pycnometer method, using benzene at 25°C . The observed density was 9.03 g/cm^3 , compared with 8.91 g/cm^3 calculated for $Z = 2$.

Resistivity measurements by the four-probe method were made on two crystals from two separate preparations. Metallic behavior was observed from 4.2°K ($\rho \sim 10^{-5} \text{ ohm-cm}$) to room temperature ($\rho \sim 10^{-4} \text{ ohm-cm}$). Thermoelectric power measurements at room temperature gave a Seebeck coefficient versus copper of $+1.6 \mu\text{V}/^\circ\text{C}$.

Magnetic susceptibility measurements at 298° , 77° , and 4.2°K were made with a Faraday balance. Between fields of 1×10^3 and $8 \times 10^3 \text{ Oe}$, the expression $\chi_m = \chi_m^0 + a/H$ was followed very well. The values of $\chi_m^0 \times 10^3$ and a , respectively, were: 0.25 and 0.52 at 298°K , 0.43 and 2.15 at 77°K , and 2.34 and 0.65 at 4.2°K . The observed field dependence could easily be due to a very small amount of an unknown ferromagnetic contaminant.

The unit cell edge of $\text{La}_4\text{Re}_6\text{O}_{19}$ was determined by use of a Guinier camera using strictly monochromatic CuK_α radiation. A potassium chloride internal standard was used, and a least-squares refinement was carried out. At 25°C the unit cell edge is $9.0308(2) \text{ \AA}$.

Although single crystals were available, it was decided that x-ray intensity data from $\text{La}_4\text{Re}_6\text{O}_{19}$ powder might lead to a structure just as reliable as that determined from single

crystal data, due to the difficulty of completely correcting for the high absorption of the compound in the single crystal case. Integrated intensity powder data were therefore gathered with a Norelco diffractometer using $\text{CuK}\alpha$ radiation and a LiF bent crystal monochromator.

The polarization factor used in the structure calculations was $(1 + \cos^2 2\theta_m \cos^2 2\theta)/2$, where θ_m is the monochromator angle (22.5° in this case). The scattering factor for O^{2-} was taken from Tokonami.⁶ The scattering factors for neutral La and Re, as well as anomalous dispersion corrections for La, Re, and O, were taken from Cromer.⁷ Initial computations for structure determination and refinement were made using a program developed by Raccach and Goodenough.⁸ Trial atomic positions for La and Re, obtained on the basis of composition and geometrical considerations within the possible space groups $\text{I}2_13$, $\text{I}23$, and $\text{Im}3$, established the space group to be $\text{I}23$.

TABLE III-4
ATOMIC POSITIONAL AND ISOTROPIC
THERMAL PARAMETERS* FOR $\text{La}_4\text{Re}_6\text{O}_{19}$

Atom	Position	x	y	z	B
La	8(c)	0.1613 (4)	0.1613	0.1613	-0.04 (11)
Re	12(e)	0.3659 (4)	0.5	0.0	-0.02 (3)
O_1	12(d)	0.331 (5)	0.0	0.0	0.97 (99)
O_2	24(f)	0.340 (4)	0.272 (4)	0.979 (5)	1.24 (83)
O_3	2(a)	0.0	0.0	0.0	-4.85 (279)

* Parameters are expressed as fractions of the unit cell edge. Standard deviations are in parentheses.

The final refinements were performed using a least-squares program written by C. T. Prewitt.* All possible reflections which occurred for $15^\circ < 2\theta < 160^\circ$ were used. Real and imaginary anomalous dispersion corrections were made for all atoms. Based on 56 reflections, the final value of the parameter R was 0.027, where $R = \sqrt{\sum(I_o - I_c)^2 / \sum I_o^2}$, I_o is the observed intensity, and I_c is the calculated intensity. The corresponding value of R' was 0.038, where $R' = \sum |I_o - I_c| / \sum I_o$. The final values of the atomic parameters are given in Table III-4. Bond distances and angles were then calculated using a program written by L. W. Finger.* Some of the distances are given in Table III-5.

$\text{La}_4\text{Re}_6\text{O}_{19}$ is a three-dimensional network, as shown in Fig. III-4, in which rhenium-oxygen octahedra share edges in pairs and are further linked by sharing corners. In each pair, as shown in Fig. III-5, across the shared edge there is a short Re-Re distance of 2.42 \AA which is presumably associated with a homopolar metal-metal bond. The Re-Re distance in rhenium metal is 2.75 \AA , and according to Cotton⁹ a distance of 2.42 \AA would correspond approximately to a double bond.

* E. I. DuPont de Nemours and Company.

TABLE III-5 BOND DISTANCES IN $\text{La}_4\text{Re}_6\text{O}_{19}$			
Bond	Distance (Å)	Bond	Distance (Å)
Re-Re	1×2.422	La-O _{1a}	3×2.567
	4×3.519	La-O _{2a}	3×2.513
Re-O _{1a}	2×1.948	La-O _{2b}	3×2.934
Re-O _{2a}	2×1.913	La-O ₃	1×2.523
Re-O _{2b}	2×2.081		

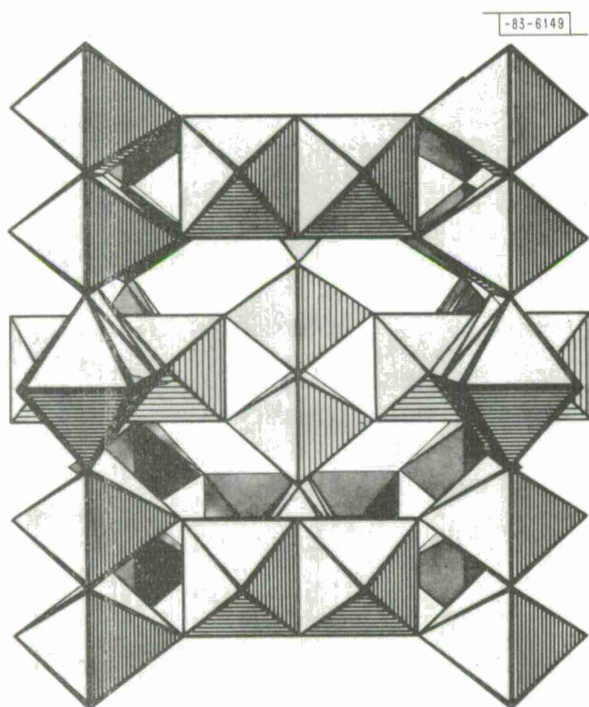


Fig. III-4. Network of rhenium-oxygen octahedra in $\text{La}_4\text{Re}_6\text{O}_{19}$.

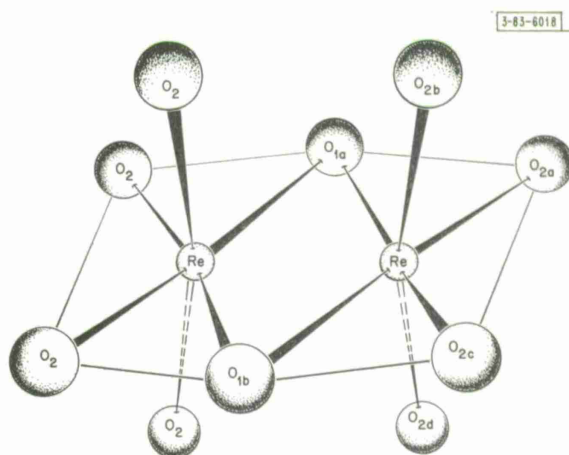


Fig. III-5. Rhenium-oxygen octahedra pair in $\text{La}_4\text{Re}_6\text{O}_{19}$.

The network of rhenium-oxygen octahedra contains sizable voids, within which there are La_4O tetrahedra centered at the origin and at the body center. The lanthanum-oxygen coordination is probably best described as a trigonal prism which is capped on all three rectangular faces and one triangular face.

The compounds KSbO_3 (Ref. 10) and KBiO_3 (Ref. 11) are reported to have the same type of octahedral network as shown in Fig. III-4, but the voids are occupied in a different manner. The bonding in the network is undoubtedly highly covalent in these compounds as well as in $\text{La}_4\text{Re}_6\text{O}_{19}$. This is particularly evident from the short oxygen-oxygen distances between those oxygen atoms making up the octahedron around rhenium. Some of these distances are less than twice the ionic radius of O^{2-} but are consistent with oxygen-oxygen distances found in certain covalent oxides.

The formal oxidation state of rhenium in $\text{La}_4\text{Re}_6\text{O}_{19}$ is $+4\frac{1}{3}$. This implies that if the rhenium atoms are all equivalent, delocalization of some electrons must occur. The electrical resistivity data clearly indicate that delocalization has taken place. This conclusion is further supported by the low Seebeck coefficient, which is typical of metals, and by the very low, nearly temperature-independent magnetic susceptibility.

J. M. Longo
A. W. Sleight*
D. A. Batson

E. PREPARATION OF TRANSPARENT FERRIMAGNETIC MATERIALS

Single crystals of RbNiF_3 , a transparent ferrimagnetic compound with a transition temperature of about 140 °K (Refs. 12 and 13), have been grown from the melt by the Bridgman method. The starting material was prepared at 1000 °C in graphite crucibles by the following exchange reaction:¹² $3\text{RbF} + \text{NiCl}_2 = \text{RbNiF}_3 + 2\text{RbCl}$. Differential thermal analysis measurements show that the compound melts at about 980 °C and exhibits a second order phase transition at 705 °C. Since the vapor pressure at the melting point is not appreciable, single crystal growth by the Czochralski method appears feasible.

Faraday rotation data^{13,14} for visible and near infrared wavelengths suggest that RbNiF_3 may be useful in isolators for laser radiation in these spectral regions. In order to study the possibility of using the material as an isolator for CO_2 lasers, the transmission of a sample 3 mm thick was measured between 2 and 15 μm . No electronic transitions associated with the Ni^{2+} ion were observed in this region. The transmission was about 90 percent between 2 and 7.5 μm , where it began to decrease because of lattice absorption. At 10.6 μm , the wavelength of the CO_2 laser, the transmission was 37 percent, corresponding to an absorption coefficient of about 4 cm^{-1} . No appreciable transmission was observed beyond 12 μm .

The compound TlNiF_3 has the same structure as RbNiF_3 and is ferrimagnetic below 150 °K (Ref. 15). Its transmission at 10.6 μm should be higher than that of RbNiF_3 , since its lattice absorption at that wavelength should be smaller. Therefore an attempt has been made to prepare this compound by dissolving the metal carbonates or hydroxides in hydrofluoric acid and then firing the filtered precipitate at 350 °C in argon. Single phase TlNiF_3 was not obtained. An

* E. I. DuPont de Nemours and Company.

Section III

attempt to produce TlNiF_3 by melting the precipitate at 1000°C under 100 atm of argon was also unsuccessful, since dissociation and rapid loss of material occurred.

J. R. O'Connor M. C. Plonko
A. Ferretti A. J. Strauss

F. PROPERTIES OF MATERIALS FOR OPTICALLY-PUMPED LASERS

The optical and magnetic transitions associated with U^{+2} , U^{+3} , and U^{+4} in CaF_2 have been identified by measurements on Bridgman-grown crystals doped primarily with each of these ions. On the basis of these identifications, it has been found that $\text{CaF}_2:\text{U}^{+3}$ laser crystals usually contain significant amounts of U^{+2} and U^{+4} ions, which interact with the U^{+3} ions and increase the laser threshold. The threshold has been reduced by a factor of 4 in crystals prepared by a method which decreases both the U^{+2} and U^{+4} concentrations. This reduction in threshold is of technological interest, since $\text{CaF}:\text{U}^{+3}$ lasers can be efficiently pumped and modulated with GaAs injection diodes.¹⁶

In order to understand the effect of the crystal field on rare earth ions substituted for Y in YVO_4 , the EPR spectra of Nd^{+3} and Gd^{+3} ions in this host have been measured from 4.2° to 273°K . (Oriented single crystals for these measurements were supplied by the Linde Division, Union Carbide Corp.) Both ions are acted on by a tetragonal crystal field. In order to obtain additional data on YVO_4 and other rare earth vanadates, a high temperature furnace is being constructed for growing single crystals of these compounds from the melt by the Czochralski method.

J. R. O'Connor G. B. Wright
W. C. Kernan H. J. Zeiger
J. J. Stickler

G. CHEMICAL ANALYSIS

1. X-ray Fluorescence Analysis of $\text{W}_{1-x}\text{Re}_x\text{O}_3$ Solid Solutions

An x-ray fluorescence method has been developed for the determination of tungsten and rhenium in $\text{WO}_3\text{-ReO}_3$ solid solutions. A powdered sample weighing 50 mg is decomposed in a flux of 5 g each of sodium carbonate and sodium borate. Before fluxing, ErCl_3 is added for use as an internal standard. The flux cake plus decomposed sample is ground to powder and then pressed to form a $\frac{1}{2}$ -in. diameter pellet. This pellet is placed in the center of a $1\frac{1}{4}$ -in. diameter pellet mold, where it is surrounded and covered with boric acid. On pressing, the boric oxide forms a supporting container for the sample pellet. Standard samples are made by decomposing in the flux suitable quantities of WO_3 , ReO_3 , and ErCl_3 of known assay.

The fluorescence spectra of the standards and samples are excited by the radiation from a chromium x-ray tube operated at 20 kV and 25 mA. The $L_{\alpha 1}$, $L_{\alpha 1}$, and $L_{\beta 1}$ lines of W, Re, and Er, respectively, are measured with a scintillation counter, LiF analyzing crystal, air path, and pulse height analyzer. Background corrections are made, but no absorption or enhancement corrections are necessary.

The average relative error for both W and Re is about 0.5 percent.

E. B. Owens
Isabel H. Searles

2. Determination of Yttrium and Iron in Yttrium-Iron Garnets

A method has been developed for the determination of yttrium and iron in yttrium-iron garnets (YIG). The sample is decomposed by fluxing in potassium pyrosulfate and then dissolved in 20 percent sulfuric acid solution. The total yttrium plus iron is determined on an aliquot of the sample solution by adding an excess of EDTA and back titrating this excess with a standard zinc solution of pH 5.1 to an automatic, potentiometric end point.

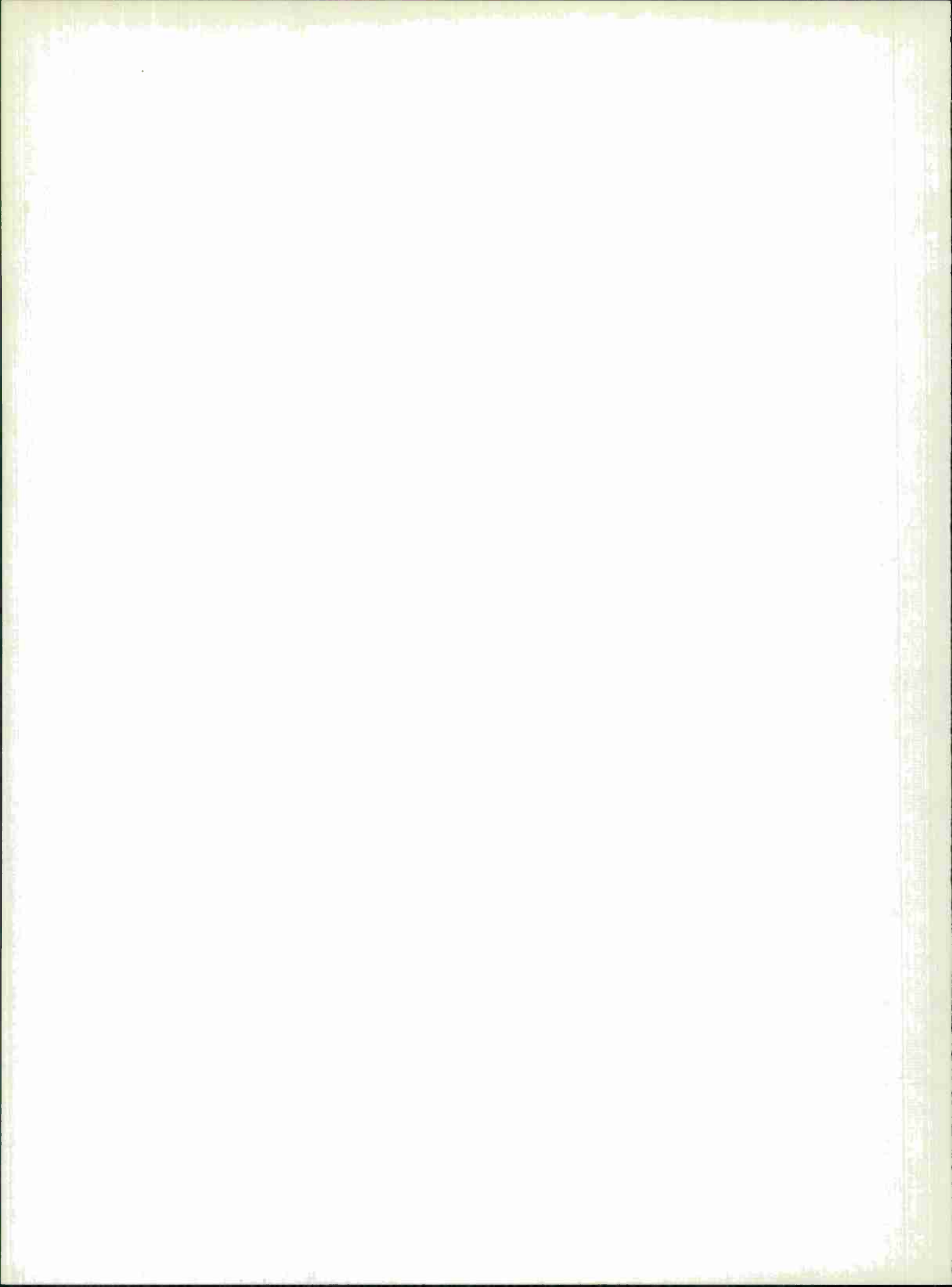
The iron is determined on a separate aliquot by the spectrophotometric, ortho-phenanthroline method.

The average relative error is 0.2 percent for the yttrium plus iron determination and 0.5 percent for the iron determination.

E. B. Owens
D. J. Soracco

REFERENCES

1. A. Mitchell, *Nature* 201, 390 (1964).
2. I. Tsubokawa, *J. Phys. Soc. Japan* 15, 1664 (1960).
3. G. Brauer, *Handbook of Preparative Inorganic Chemistry* (Academic Press, New York, 1963), Vol. 2, p. 1314.
4. Solid State Research Report, Lincoln Laboratory, M. I. T. (1967:2), DDC 656548.
5. J. M. Longo, "Some New Ternary Oxides of Rhenium," PhD. thesis, Dept. of Chemistry, University of Connecticut, 1964.
6. M. Tokonami, *Acta Cryst.* 19, 486 (1965).
7. D. T. Cromer, *Acta Cryst.* 18, 20 (1965).
8. P. M. Raccah and J. B. Goodenough, *Phys. Rev.* 155, 932 (1967).
9. F. A. Cotton, *Chem. Soc. Quart. Rev.* 20, 389 (1966).
10. P. Spiegelberg, *Arkiv Kemi* 14A, No. 5 (1940).
11. J. Zemann, *Tschermaks Mineral. Petrog. Mitt.* 1, 361 (1950).
12. G. A. Smolenskii, V. M. Yudin, P. P. Syrnikov, and A. B. Sherman, *Soviet Phys. - Solid State* 8, 2368 (1967).
13. M. W. Shafer, T. R. McGuire, B. E. Argyle, and G. J. Fan, *Appl. Phys. Letters* 10, 202 (1967).
14. R. V. Pisarev, I. G. Sinii, and G. A. Smolenskii, *Soviet Phys. JETP Letters* 5, 79 (1967).
15. K. Kohn, R. Fukuda, and S. Iida, *J. Phys. Soc. Japan* 22, 333 (1967).
16. R. J. Keyes and T. M. Quist, *Appl. Phys. Letters* 4, 50 (1964).



IV. PHYSICS OF SOLIDS

A. ELECTRONIC BAND STRUCTURE

1. Analysis of Shubnikov-de Haas Results for HgSe

In a previous report¹ we discussed two explanations for the Shubnikov-deHaas (SdH) data on n-type HgSe taken by Whitsett.² In addition to a nearly isotropic, main SdH frequency, Whitsett observed a beat frequency when the magnetic field, \vec{H} , was along all directions of the (110) plane except when parallel to $\langle 110 \rangle$. With the use of Kane's³ expression for Γ_6 and Γ_8 conduction bands, we showed that the beating effect could, in principle, be caused by either the warping term or the inversion asymmetry term. The warping term explanation was rejected because: first, the large amount of warping required to produce a beat frequency² was hard to reconcile with the systematic behavior of the band structure of the diamond-zincblende semiconductor family; and secondly, the required warping would cause a 20 percent difference in the main SdH frequencies between $\langle 111 \rangle$ and $\langle 100 \rangle$ orientations while, in fact, a maximum variation of 7 percent and a typical variation of 3 or 4 percent were observed.

We showed that the size of the inversion asymmetry splitting required to account for the beating was quite reasonable: Kane's parameter B or G must be 6, in units of $\hbar^2/2m_0$, for a Γ_8 conduction band and twice that for a Γ_6 conduction band.[†] For a sample with 1.3×10^{18} electrons/cm³ the Fermi energy is about 0.13 eV and the maximum inversion asymmetry splitting (occurring along $\langle 110 \rangle$) is about 7 meV.

The zero field constant energy orbits with the inversion asymmetry splitting are shown in Fig. IV-1 for $k_3 = 0$ and k_3 along three principal directions. Since the SdH frequencies are

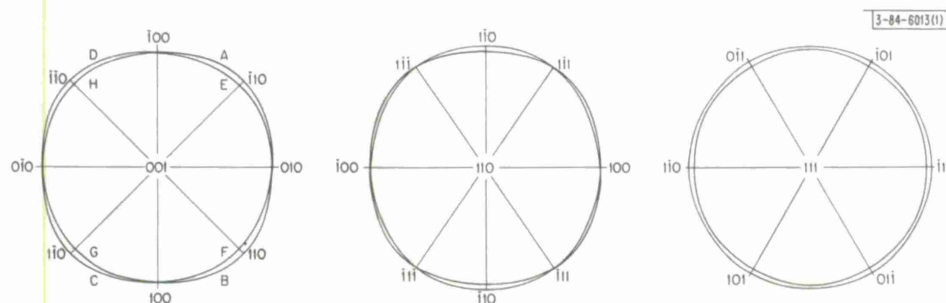


Fig. IV-1. Constant energy surfaces with inversion asymmetry splitting for $k_3 = 0$, with k_3 along [001], [110] and [111] directions.

proportional to the extremal areas generated by orbits perpendicular to the magnetic field, it is reasonable that two nearly equal frequencies do appear for \vec{H} along $\langle 111 \rangle$. However, one cannot similarly conclude on this basis from Fig. IV-1 that two frequencies exist for \vec{H} along $\langle 100 \rangle$ and only one frequency for \vec{H} along $\langle 110 \rangle$, as is observed experimentally.

[†] It was incorrectly stated in Ref. 1 that this parameter is ten, not two, times as large.

Section IV

Recently, Professor Laura Roth of Tufts University, using a 2×2 effective Hamiltonian which includes the inversion asymmetry term, has been able to show that the magnetic field causes an interaction between the orbits for \vec{H} along $\langle 100 \rangle$ but not for \vec{H} along $\langle 110 \rangle$. This splits the orbit degeneracies for the $\langle 100 \rangle$ case, and at sufficiently high fields two SdH periods corresponding to the outer and inner areas should be observed. This process is the reverse of magnetic breakdown in the sense that, instead of the magnetic field causing transitions across zero field energy gaps, the magnetic field introduces a gap which alters the zero field orbits. When the breakdown criterion is applied to this case, it is found that at 10 kG, where Whitsett first observed the beating, incomplete reverse breakdown is likely to be occurring and the zero field area, [AFCH] in Fig. IV-1, is beating against an area traced out by an electron switching at two of four junctions (such as orbit [ABCH]). This produces a $\langle 100 \rangle$ beat frequency which is about $1/4$ of that for $\langle 111 \rangle$, and gives rise to minima, rather than nodes, in the amplitude. It is not possible to get more than an upper limit on the $\langle 100 \rangle$ beat frequency from Whitsett's data, but, for this direction, minima rather than nodes do seem to be observed.

A report of the progress on this problem has been written with Professor Roth and submitted for publication. Several interesting theoretical and experimental problems remain: It would be desirable to get exact quantum mechanical solutions of the 2×2 magnetic Hamiltonian, thus bypassing the magnetic breakdown arguments which are more suitable for well separated metallic-like orbits, with only one or a few points of close approach, than for the orbits shown in Fig. IV-1. A new effort to determine a full $\langle 100 \rangle$ period for HgSe seems worthwhile, as does an attempt to obtain homogeneous n-type HgTe in hopes of seeing similar beating effects for that material.

S. H. Groves
P. W. Wyatt†

2. Warping-Induced Transitions in InSb

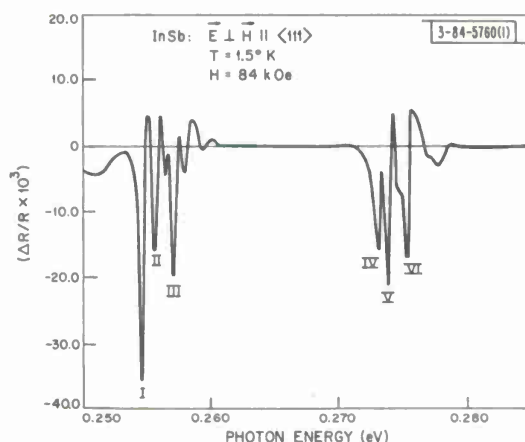
Figure IV-2 shows the Faraday configuration transitions to the $n = 0$ conduction band levels in InSb, with the magnetic field along $\langle 111 \rangle$. In addition to the "allowed" transitions, I, III, IV and V, which may be seen for \vec{H} along all directions, it is possible to see two extra transitions, II and VI. These are identified as "warping induced" and are of about the same strength as the allowed transitions. They appear for \vec{H} along $\langle 111 \rangle$ but not along $\langle 110 \rangle$ or $\langle 100 \rangle$ and are absent when the reflecting surface is a (100) or (110) plane. The trace in Fig. IV-2 was obtained using electric field modulated magnetoreflexion but the extra transitions can readily be seen in ordinary magnetoreflexion as well.

Figure IV-3 shows the Landau levels near the band edge in InSb with the transitions (Roman numerals) of Fig. IV-2 and the polarizations in which they are seen. The labeling of the levels and ladders follows the notation of Luttinger.⁴ The parentheses give the components of the wave function. For example, $(1/\sqrt{2}) (-1/2, 2) + (1/\sqrt{2}) (3/2, 0)$ denotes the wave function $\psi = (1/\sqrt{2}) u_{-1/2} \varphi_2 + (1/\sqrt{2}) u_{3/2} \varphi_0$, where u_m is a band edge Bloch function of M units of angular momentum along \vec{H} , and φ_n is the one dimensional harmonic oscillator function of order n .

From the energy and polarization dependence of the extra transitions we conclude that they must come from terms, omitted from the magnetic Hamiltonian to make it exactly solvable,⁴ which connect the close lying states $a^-(2)$ and $b^+(0)$, shown by the heavy arrow in Fig. IV-3. Normally,

† Yale University.

Fig. IV-2. Lowest transitions in the InSb magneto-electroreflectance spectrum for both σ_r and σ_l Faraday configurations.



the omitted terms are unimportant; however, if they connect nearly degenerate levels, the wave functions can become sufficiently admixed so that extra transitions are observed. It is not uncommon to observe extra transitions the size of the small structure of Fig. IV-2, but seldom is the admixing so complete as to give transitions of the size of II and VI.

Two terms connecting the desired levels can be found from Luttinger's work:⁴

$$\sqrt{\frac{3}{4}}(\gamma_3 - \gamma_2) f(\Theta) [n(n-1)]^{1/2} \quad \text{between } u_{-1/2}\varphi_n \text{ and } u_{-3/2}\varphi_{n-2}$$

and

$$\frac{3}{8}qf(\Theta) \quad \text{between } u_{3/2}\varphi_n \text{ and } u_{-3/2}\varphi_n$$

Θ is the angle between $[001]$ and \vec{H} , where \vec{H} is taken to lie in the $(1\bar{1}0)$ plane. $f(\Theta)$ is $\sin\Theta \cos\Theta(3\cos^2\Theta - 5)$, which vanishes for H along $[001]$ ($\sin\Theta = 0$), for \vec{H} along $[1\bar{1}0]$ ($\cos\Theta = 0$)

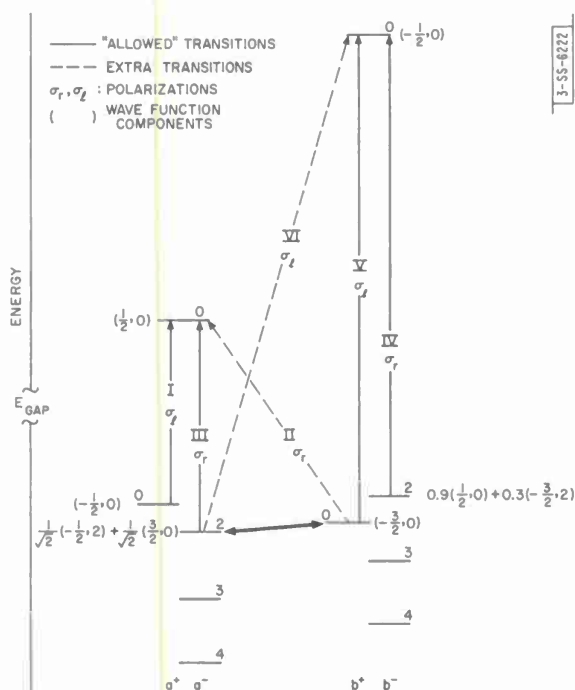


Fig. IV-3. Schematic representation of uppermost valence band and lowermost conduction band Landau levels in InSb.

but not for \vec{H} along $[1\bar{1}1]$ ($\sin\theta = \sqrt{2/3}$, $\cos\theta = \sqrt{1/3}$). Thus, the two terms which connect the desired levels also have the angular dependence which is found experimentally.

The quantity $(\gamma_3 - \gamma_2)$ is a measure of the warping of the valence band energy surfaces, and has been determined to be about 1, in units of $\hbar^2/2m_0$, for InSb from cyclotron resonance.⁵ This and the unperturbed energy separation of the $a^-(2)$ and $b^+(0)$ can be used to calculate the strength of the extra transitions. When this is done, good agreement with the observed strength is found.

The quantity q has been estimated to be very small for Ge, but it depends upon the spin-orbit splitting and should be considerably larger in InSb, which has a spin-orbit splitting about three times larger than Ge. Yet, we are unable to account for the strength of the extra transitions using the $(\gamma_3 - \gamma_2)$ term and can only say that q is smaller than $(\gamma_3 - \gamma_2)$ for InSb.

S. H. Groves
C. R. Pidgeon†

3. Magneto-Electroreflectance of InAs and InSb at Liquid Helium Temperature

Work has been completed on the magneto-electroreflectivity study of transitions from the split-off valence band to the conduction band in InAs and InSb, at 1.5°K. We report the first direct experimental observation of the $\vec{k} = 0$ spin-orbit splitting in InAs ($\Delta = 0.38 \pm 0.01$ eV), as well as the effective mass ($m_{so} = 0.14 \pm 0.01 m_0$) and g-factor ($g_{so} = 13.0 \pm 1.0$) for the split-off band. For InSb we find $\Delta = 0.81 \pm 0.01$ eV, which is in good agreement with the magneto-piezoreflection results of Aggarwal.⁶ A report of this work has been accepted for publication in Solid State Communications.⁷

S. H. Groves
C. R. Pidgeon†
J. Feinleib

4. Magnetoreflexion and the Electronic Energy Bands in Bismuth

A lineshape calculation has been carried out which satisfactorily describes the oscillatory magnetoreflexivity in bismuth with H parallel to the binary direction.⁸ This calculation takes into account in a consistent manner: the simple Lax model for the nonparabolic electron energy bands;⁸ the k -dependence of the velocity matrix elements;⁹ and the anisotropic properties of the constant energy surfaces¹⁰ in the neighborhood of the L point, about which the interband transitions occur. In the course of making this lineshape calculation, it was found necessary to explore the modifications of the lineshape which arise from bands not treated in the Lax model, but which have been considered by Baraff.¹¹

Although the resonant frequencies for the magnetoreflexion experiment are found to be in excellent agreement with the Lax model, it is necessary to use the Baraff modifications to adequately describe the lineshape. As a result of this work, it has been possible to greatly simplify the Baraff model. In particular, the magnetoreflexion experiments on bismuth carried out at the National Magnet Laboratory have provided certain relations between parameters appearing in the Baraff theory. Using these relations, the formalism is sufficiently simplified so that the magnetic energy levels can be calculated at $k_H \neq 0$, i.e., away from the extrema of the Landau levels. The resulting formulas for the magnetic energy levels in bismuth near point L are given here, correct to first order in perturbation theory. The Landau level which is non-degenerate in the Lax model is labeled by $(j, s) = (0, 1)$ where j is related to $n =$ Landau level

† National Magnet Laboratory, M.I.T.

index and s = spin quantum number (± 1) by $j = n + \frac{1}{2} - s$ and the energy for this $(0, 1)$ level is given by

$$E(0, 1) = E^0(0, 1) + H\nu \left[1 - \frac{\hbar^2 k_H^2 E_g^2}{m_o m_H [2E^0(0, 1) + E_g^0] E^0(0, 1)} \right] \quad (1)$$

This level is merely shifted up or down from the Lax energy $E^0(0, 1)$ depending on whether ν is positive or negative. As for the other magnetic energy levels of the Lax model, the Baraff modification serves to remove the degeneracy of $E^0(j, s)$ according to the relation

$$E(j, s) = E^0(j, s) + H\nu s \sqrt{1 - \frac{\hbar^2 k_H^2 E_g^2}{2m_o m_H [E^0(j, s)]^2}} \quad (2)$$

the degeneracy being removed by the s -dependence of the Baraff perturbation term. In these equations k_H is the crystalline momentum parallel to H , E_g is the energy gap between the two closely coupled bands and $E^0(j, s)$ gives the s -independent magnetic energy levels of the Lax model

$$E^0(j, s) = \left[\frac{E_g^2}{4} + E_g \left(\beta^* H j + \frac{\hbar^2 k_H^2}{2m_o m_H} \right) \right]^{1/2} \quad (3)$$

in which

$$2j = 2n + 1 - 2s \quad (4)$$

and

$$\beta^* H = \frac{|e|\hbar}{m_o c} \left[\frac{\vec{H} \cdot \vec{m}^* \cdot \vec{H}}{|\vec{m}^*|} \right]^{1/2} \quad (5)$$

where m_o is the free electron mass and \vec{m}^* is the dimensionless effective mass tensor for the electrons in bismuth. The corresponding effective mass tensor \vec{m}_H describing motion along the magnetic field need not be equal to \vec{m}^* but is exactly equal to this quantity if Baraff terms are ignored. The dimensionless effective mass m_H is related to the tensor \vec{m}_H by the relation

$$m_H = \vec{H} \cdot \vec{m}_H \cdot \vec{H} / H^2 \quad (6)$$

The energy which expresses the Baraff shifts and splittings is

$$H\nu = \frac{|e|\hbar}{m_o c} \frac{\vec{H} \cdot \vec{\mathcal{F}} \cdot \vec{H}}{[\vec{H} \cdot \vec{m}^* \cdot \vec{H}]^{1/2}} \quad (7)$$

in which $\vec{\mathcal{F}}$ is a dimensionless tensor which assumes the same form as \vec{m}^* and is determined by experimental measurements.

With these simplifications, the Baraff corrections to the Lax model can be applied more readily to the interpretation of experiments sensitive to the splittings of the magnetic energy levels.

M. S. Maltz
Mildred S. Dresselhaus

Section IV

5. Low Energy Interband Transitions and Band Structure of Nickel

A Physical Review Letter¹² entitled "Low Energy Interband Transitions and Band Structure of Nickel" has been published. In this letter we analyzed a model of the band structure of nickel in which the conduction band is lowered about 1 eV with respect to the d band. This shift of the conduction band brings the L_2' conduction state below the top of the d band (L_{32}) in the [111] direction. The necks observed in the de Hass-van Alphen effect in the [111] direction in nickel and copper are now interpreted differently. In nickel the neck has a larger d character than in copper. This reordering of the bands brings all the known data into better agreement with the one electron band picture, including the interband transitions at 0.25 and 0.40 eV detected in the temperature-modulated reflectance measurements.¹³ This reordering of the bands predicts interesting properties for the Cu-Ni alloys, in particular a crossing of the L_2' and L_{32} states.

J. Hanus
J. Feinleib
W. J. Scouler

6. Symmetry of Cation d-Bands in the Corundum Structure

Cation d-bands in the corundum structure have been examined theoretically to determine possible physical implications of the symmetry, particularly for Ti_2O_3 and V_2O_3 . It is found for the nonmagnetic corundum structure (space group $D_{3d}^6(R\bar{3}c)$) that band structures are possible which are consistent with the symmetry and which represent each of the following: semiconducting Ti_2O_3 , metallic Ti_2O_3 , semiconducting V_2O_3 , and metallic V_2O_3 . A temperature-dependent two-band semiconductor model has been proposed¹⁴ recently to account for the temperature dependence of the resistivity of Ti_2O_3 .

A Brillouin zone for the corundum structure is shown in Fig. IV-4, with all points and lines of special symmetry indicated. The symbols for the points and lines of symmetry are those of Cohen.¹⁵ These are correlated as follows with the symbols used by Slater¹⁶ who indicates the points and one of the lines (Cohen-Slater): Γ - Γ , Λ - Λ , Σ - Δ , T - Z , L - A , X - B , Y - Δ' . The reflection plane σ lies in the xz plane normal to the binary axis along y. Figure IV-5 shows schematically the parts of the energy bands pertinent for determining the semiconducting or metallic character of the band structure. Traces along only the trigonal axis, line $\Gamma\Lambda T$, are shown, and the degeneracy of a level is indicated by an encircled number. Spin-orbit coupling and spin

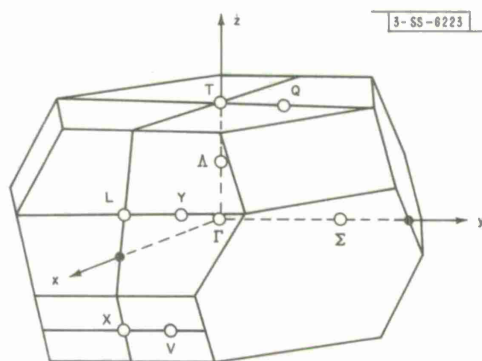


Fig. IV-4. Brillouin zone for rhombohedral Bravais lattice with all points and lines of special symmetry indicated for space group $D_{3d}^6(R\bar{3}c)$.

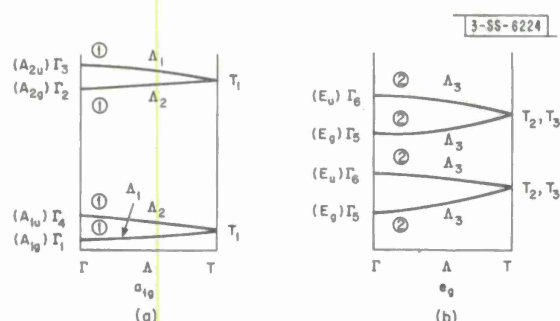


Fig. IV-5. Energy bands for the corundum structure arising from (a) a_{1g} cation orbitals and (b) e_g cation orbitals.

est in energy and with maximum charge density in the directions of the octahedron of nearest neighbor anions, and $e_g(\pi)$, lying lower and with maximum charge density transverse to the trigonal axis.

The rhombohedral unit cell contains four cations and six anions, so that each cation orbital gives rise to four bands – 20 d-like bands in all. The four bands arising from an a_{1g} localized orbital are indicated in Fig. IV-5a. Symmetry requires that these bands touch in pairs at the point T. Shown similarly in Fig. IV-5b are the eight bands, doubly degenerate in pairs at Γ , arising from a localized e_{g1} , e_{g2} orbital pair. In this case spatial symmetry requires these bands to remain degenerate along the line Γ AT. In addition, time inversion symmetry requires the T_2 bands and the T_3 bands to be degenerate in pairs. An examination was made of the implications of any similar symmetry-induced degeneracy of the bands occurring elsewhere within or on the surface of the Brillouin zone (see Fig. IV-4) with the following conclusion: No additional consequences of symmetry force removal of any of the remaining energy gaps. These results were obtained with the aid of tables¹⁶ of irreducible representations of the groups of the k -vector for the space group D_{3d}^6 .

If spin is taken into account, some of the band degeneracy may be removed by spin-orbit coupling, but no further touching between the no-spin bands can be required by symmetry. This can be understood by introducing the spin-orbit coupling as a perturbation λH_{s-o} and increasing the strength parameter λ between 0 and 1; any symmetry consequences of spin-orbit coupling must appear already for λ small.

Each band (such as in Fig. IV-5) can accommodate two electrons per rhombohedral unit cell.

It is, of course, easy to imagine a band structure representing a metal for any number of d-electrons per cation except 0 or 10; it is only necessary that the bands have enough overlap among themselves. It is also easy to synthesize a band structure to represent semiconducting Ti_2O_3 , which has one 3d electron per Ti^{+++} ion outside an argon-like core. Consistent with symmetry, the Γ_1 and Γ_4 bands are put lowest, to just accommodate the four electrons per unit cell, and are separated from the remaining 18 d-bands by an energy gap. By putting the Γ_2 and Γ_3 bands next, an insulator could be made out of V_2O_3 , which contains eight electrons per unit cell to be accommodated by the d-like bands. It is more plausible, however, to put one of the four $\Gamma_5 - \Gamma_6$ band complexes next, instead. This arrangement of the bands accounts for the metallic character of V_2O_3 at high temperatures, and is apparently also consistent with the

Section IV

observed metal-to-semiconductor transitions^{17,18} near 150°K in that it allows a gap to be formed in the $\Gamma_5 - \Gamma_6$ band complex when the symmetry is lowered at the transition.

Symmetry determines the symmetry types of the bands in Fig. IV-5 as indicated, but does not determine their order in energy. However, if one considers the disposition along the trigonal axis of the four cations in a unit cell, as in Fig. IV-6, and if one uses a tight-binding approach to

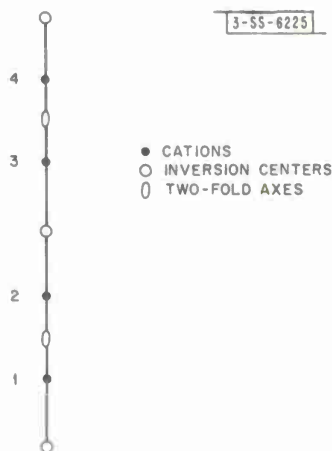


Fig. IV-6. Four cations, inversion centers, and twofold axes in a rhombohedral unit cell of the corundum structure.

describe the d-bands (which seems reasonable), then Γ_1 and Γ_4 are bonding whereas Γ_2 and Γ_3 are antibonding with respect to nearest neighbor cation pairs. On the other hand, Γ_1 and Γ_2 (Γ_3 and Γ_4) are bonding (antibonding) with respect to next nearest neighbor cations along the trigonal axis. This consideration was used in selecting the relative positions of the $\Gamma_1\Gamma_2\Gamma_3\Gamma_4$ bands in Fig. IV-5(a). The relative positions of the e_g bands in Fig. IV-5(b) were chosen similarly. This consideration suggests also that a $\Gamma_5 - \Gamma_6$ band complex is, indeed, more stable than the $\Gamma_2 - \Gamma_3$ band pair, consistent, as indicated above, with the observed metal-to-semiconductor transition in V_2O_3 .

W. H. Kleiner

B. MAGNETISM

Critical temperature measurements have been made in $\text{La}_{0.5}\text{Sr}_{0.5}\text{CoO}_3$, a cubic perovskite which exhibits metal-like electrical resistivity behavior and is ferromagnetic below 228°K. We have investigated the magnetic properties of this material at and immediately above the critical temperature in order to determine the critical point exponents γ and δ . The exponent γ is defined by the equation

$$\chi_0 \sim A(T - T_c)^{-\gamma} \quad \text{as} \quad T \rightarrow T_c^+ \quad (8)$$

which describes the nature of the divergence of the initial paramagnetic susceptibility at the Curie temperature T_c . A is a proportionality constant.

Using the method of data analysis proposed by Kouvel and Fisher,¹⁹ we obtained $\gamma = 1.27 \pm 0.02$. This is well below the value 1.40 calculated on the basis of a high temperature expansion by Stanley.²⁰ It is also significantly lower than the value $\gamma = 4/3$ which has been found in nickel,¹⁹ iron and its alloys²¹ and several other materials.²² The only cubic ferromagnetic material for which a value other than $4/3$ has previously been reported is f.c.c. cobalt, for which $\gamma = 1.21$ (Ref. 23).

The exponent δ is defined by the relationship

$$H_i \propto \sigma^\delta \quad \text{at } T = T_c, \quad (9)$$

where H_i is the magnetic field, corrected for demagnetization effects, and σ is the magnetization. We find $\delta = 3.05 \pm 0.06$, which appears to agree with the molecular field theory prediction that $\delta = 3$. However, this agreement is fortuitous since molecular field theory also predicts $\gamma = 1$.

Previous work on nickel, for which $\delta = 4.2$ (Ref. 1), had led to speculation²⁴ that there might be some depth to the analogy between magnetic properties and the behavior of a gas near its critical point. In particular, the pressure p and density ρ in a gas, measured with respect to their critical values p_c and ρ_c are related by $|p - p_c| \propto |\rho - \rho_c|^{\delta'}$. Widom and Rice²⁵ found $\delta' = 4.0 - 4.2$ in several gases, but a more recent evaluation indicates the value of δ' should be closer to 5.0 (Ref. 26). Either of these values differs sufficiently from the value of δ obtained on $\text{La}_{0.5}\text{Sr}_{0.5}\text{CoO}_3$ to dispute the generality of the analogy.

N. Menyuk
P. M. Raccach
K. Dwight

C. LASER EXPERIMENTS

1. Polarization and Intensity of Raman Scattering From Plasmons and Phonons in Gallium Arsenide

Raman scattering from plasmons and phonons in GaAs has recently been reported²⁷ in which the coupling between the longitudinal optic phonon modes and the longitudinal plasma modes was demonstrated. We have investigated the polarization properties and relative intensities of the Raman scattered laser light from mixed plasmon-phonon modes in oriented single crystals of GaAs. The results are in good agreement with theoretical predictions²⁸ and yield values for the Raman tensor and electro-optic coefficient of GaAs.

Figure IV-7 is a plot of the Raman frequency shifts as a function of the square root of the electron concentration and shows the mixing between the longitudinal optic phonon mode of frequency ω_l and the longitudinal plasma mode of frequency $\omega_p = (4\pi n e^2 / \epsilon_\infty m^*)^{1/2}$. Here n is the electron concentration, m^* the conduction band effective mass, and ϵ_∞ the optical dielectric constant.

The Raman line shapes and polarization properties for a sample with $n = 1.9 \times 10^{18} \text{ cm}^{-3}$ are shown in Fig. IV-8. The scattering angle is 90° with the incident and scattered light along $\langle 100 \rangle$ directions. The pair of \parallel and \perp signs by each trace gives the polarization of the incident and scattered light (in that order) with respect to the plane of scattering. The transverse optic (TO) mode at 273 cm^{-1} has a true width of only about 1.5 cm^{-1} ; in these traces it is considerably instrument broadened. The traces as shown are uncorrected for system response and the gain in trace (b) is lower than in the others.

The TO mode at frequency ω_t is unaffected by the presence of the free carriers and exhibits the polarization properties predicted by group theory for a zincblende insulator.²⁹ However, the polarization properties of the upper and lower longitudinal branches, L_+ and L_- , differ markedly from those found for a pure longitudinal optic (LO) mode in semi-insulating GaAs. The latter, in accordance with group theory predictions, shows zero LO scattering in the present geometry when

Section IV

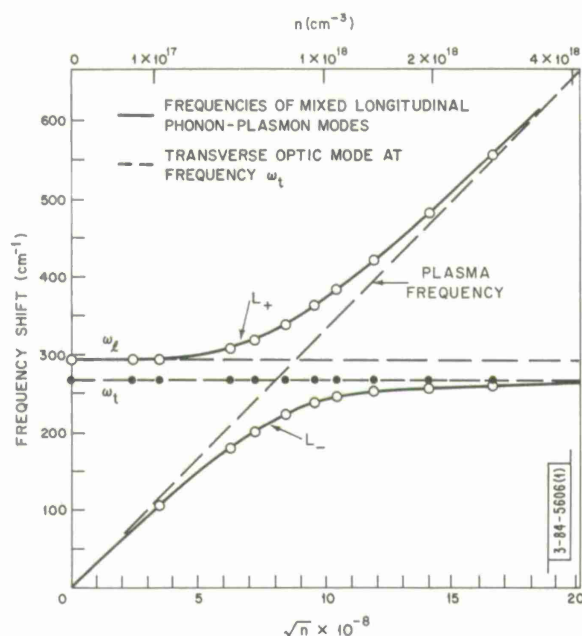


Fig. IV-7. Frequency shift of the Raman scattered light in GaAs at room temperature as a function of the square root of the electron concentration.

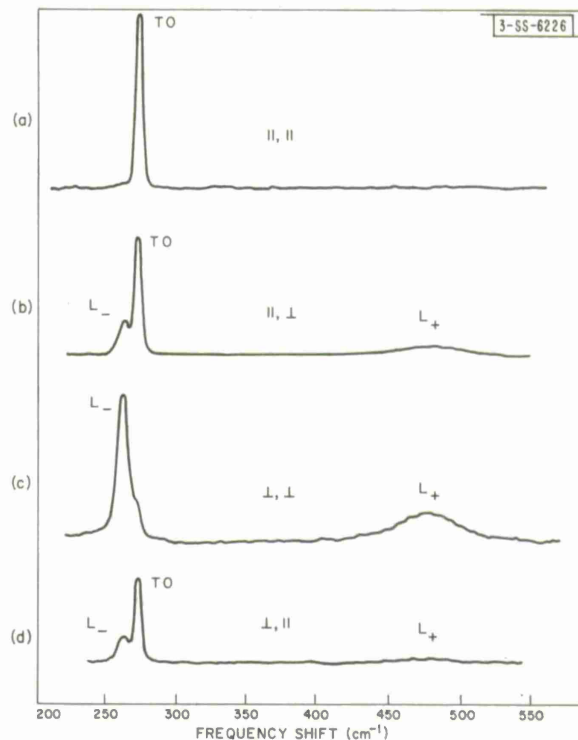


Fig. IV-8. Intensity and polarization properties of the Raman scattered light from GaAs at liquid helium temperature for a sample with $n = 1.9 \times 10^{18} \text{ cm}^{-3}$.

the incident and scattered beams are both polarized parallel to the plane of scattering ($||, ||$) or both perpendicular to the plane of scattering (\perp, \perp). But in Fig. IV-8 it is apparent that the largest longitudinal mode scattering occurs for the (\perp, \perp) configuration.[†] The strong (\perp, \perp) scattering is just what is predicted by recent theoretical calculations²⁸ which take into account the effects of charge density fluctuations.

From the theory,²⁸ the relative integrated scattering intensities for all three modes involve only the unknown Raman tensor R_{xy}^z and electro-optic coefficient z_{41} . The best fit between theory and experiment was obtained with $R_{xy}^z = 5 \times 10^{-59} \text{ cm g}^3/\text{sec}^2$ and $z_{41} = -1.0 \times 10^{-7} \text{ esu}$.

A more detailed account of this work is discussed in a forthcoming publication.³⁰

A. Mooradian
A. L. McWhorter

2. Stimulated Raman Oscillator

Further measurements have been made on the quartz Raman oscillator pumped by a ruby laser. By equating Stokes gain and cavity loss at threshold, a rough estimate can be made of the Raman susceptibility and cross section. From the threshold power density of 3 MW/cm^2 for a 1-cm sample focused by a 5-cm lens (10-mrad beam divergence), and a cavity loss per cm, $\alpha = \pi n \Delta \nu_c = 1/2L$, where n is the index of refraction and $\Delta \nu_c$ is the cavity linewidth, we calculate $\alpha \cong 0.5 \text{ cm}^{-1}$ and a gain $G \cong 1 \text{ cm}^{-1}$ or $1 \times 10^{-9} \text{ cm}^{-1}$ per watt/cm² in the estimated active path. Then $\chi^R = G/2\pi E_L^2 k_s = 1.5 \times 10^{-12} \text{ erg}^{-1} \text{ cm}^3$. This may be compared with the

[†] The dominance of the (\perp, \perp) scattering in Fig. IV-8 is actually somewhat exaggerated by the system response.

nonresonant third-order susceptibility of 1×10^{-14} obtained in mixing experiments in quartz.³¹ This larger magnitude of the resonant process seems reasonable in view of the Q of the Raman vibrational mode, $Q = \nu/\Delta\nu = 467 \text{ cm}^{-1}/2 \text{ cm}^{-1} \cong 200$. The Raman cross section is then

$$\sigma = \frac{16\pi^2 \chi_k^2 R_s \epsilon \hbar \Delta\nu_a}{N\lambda^3} = 5 \times 10^{-31} \text{ cm}^2$$

P. E. Tannenwald
F. H. Perry

3. Frequency Smearing in Nd:Glass Laser Filaments†

It has been observed that a 50-MW Nd:glass laser beam passing through a CS_2 liquid cell is spectrally broadened so that the frequencies mix in a rotatable KDP crystal to produce a wide range of continuously tunable sumfrequencies.³² This has suggested direct observation of the spectral emission from such liquids in the forward direction at high power levels. A rotating prism Q-switched 120-MW Nd:glass laser emitting a 2-cm diameter beam, which was telescoped to a 1-cm diameter, was used as a source. The spectral analysis was done with a Hilger-Watts glass prism spectrograph of $\approx 100 \text{ \AA/mm}$ dispersion in the infrared (courtesy of M. Weinreb, National Aeronautical Space Administration Electronic Research Center, Cambridge, Mass.) whose slits were protected by laser attenuating filters. The spectrum for frequencies below the laser frequency was stronger than for the higher frequencies. However, adequate spectrograms for the lower frequencies could not be taken, even with sensitized 1-Z plates, because the relative spectral sensitivity of the emulsion is too unfavorable. Higher frequency spectra were obtained in CS_2 cells with sensitized 1-M plates and are shown in Fig. IV-9. In this figure the "halo" is due to scattered laser light. Microdensitometer traces were also taken with a resolution of $\approx 50 \mu$, and the spectral characteristics of the attenuating filter, the spectrograph, and the film were taken into account. Figure IV-10(a) shows the results for CS_2 as a function of peak power for an 8-cm cell length, where the power is varied with attenuating filters in front of the liquid cell to change the power without changing the mode structure radically. All spectra have been normalized to 100 at 1.04μ . Figure IV-10(b) shows similar results for CS_2 as a function of cell length for peak powers of $90 \pm 10 \text{ MW}$. The slit width was 160μ .

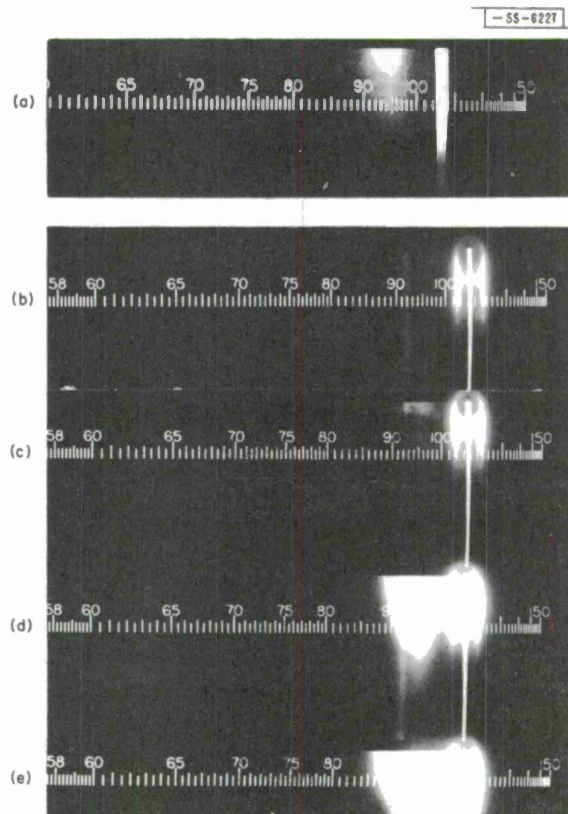


Fig. IV-9. Typical spectrograms taken with a Hilger-Watts prism spectrograph; Corning 1-69 attenuating filter for (a); Corning 7-69 attenuating filter for (b), (c), (d), and (e); and sensitized 1-M plates with slits of 160μ . Numbers correspond to 100 \AA/unit .

† Experimental work done at the National Aeronautics and Space Administration Electronics Research Center in Cambridge.

Section IV

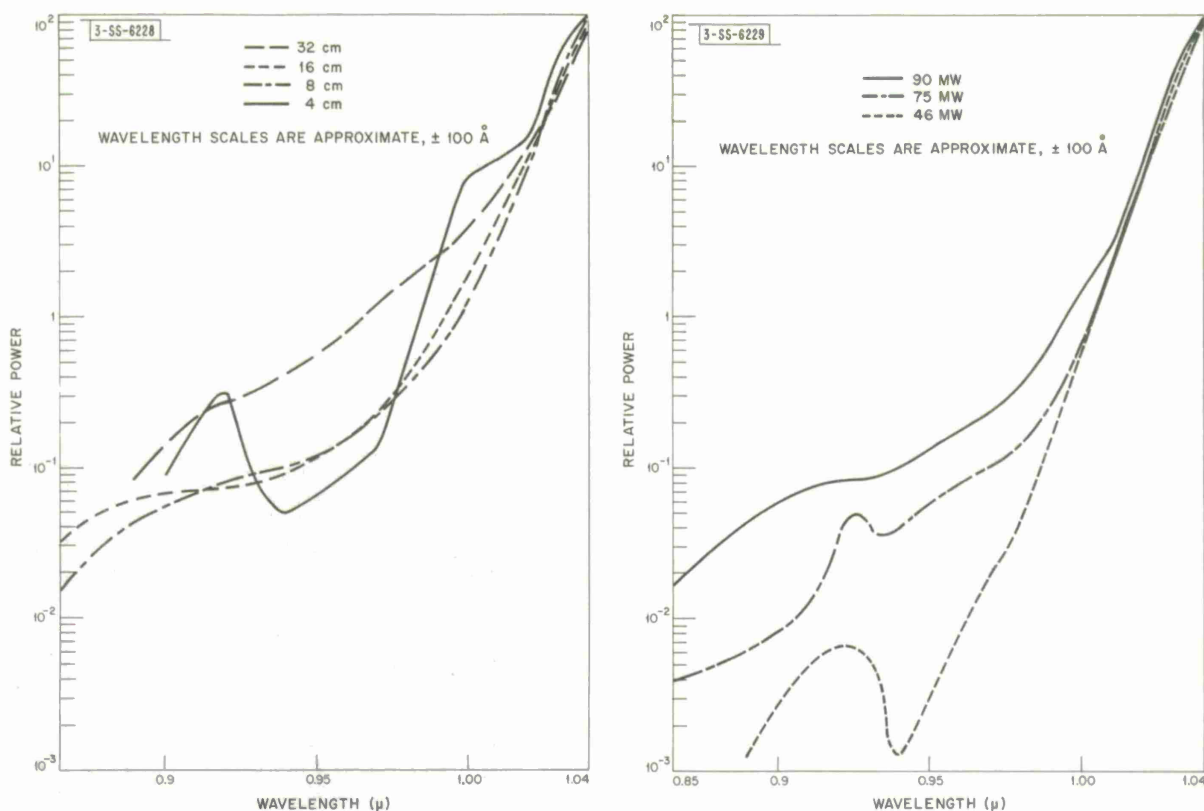


Fig. IV-10. CS₂ cell output spectrum vs line width normalized to 100 at 1.04 μ and with instrumental spectral responses removed. (a) Input laser power as a parameter for 8-cm cell length. (b) Cell length as a parameter at 90 ± 10 MW input laser power.

Several qualitative statements can be made about these results. First, sufficient frequency smearing of high enough power/bandwidth does exist in the output of the CS₂ cell to adequately explain the previously reported work.³² This spectral broadening appears to be a consequence of self-focusing and small scale trapping of intense laser light into filaments of $\approx 5 \mu$ diameter. The power densities are now so high that stimulated scattering processes and parametric beating as well as self-steepening³³ set in, which results in frequency smearing. Second, even for input powers of 100 MW at power densities of several hundred MW/cm², a frequency smeared, but Raman-like, spectrum does exist for short enough cell lengths. However, as the cell length is increased, all remnants of a Raman spectrum disappear and are replaced by a smooth, extensively smeared and relatively flat power spectrum whose power/bandwidth keeps increasing with input power. Third, the periodic sequence of lines spaced $\sim 10 \text{ cm}^{-1}$ apart, reported by R. Brewer³⁴ and C.H. Townes and co-workers³⁵ for the case of ruby laser excitation, appears to be absent for the case of Nd:glass laser excitation, for which the resolution on the plates was comparable to or less than the line spacing. This is expected because the laser linewidth is comparable to the expected spectral structure.

Work with nitrobenzene shows similar results except for less smearing and the power/bandwidth for comparable conditions. Also spectra were taken of the backward going light from the

CS₂ cell, but light was only present at the laser line (probably Brillouin or Rayleigh components). The lack of other spectral features may be due to the sensitivity decrease caused by the more complex arrangement required.

R. L. Carman

4. Far Infrared Cyanide Laser

Satisfactory routine operation has been achieved. Water cooling is superior to air cooling with respect to laser amplitude stability and lifetime of discharge tube. The 337 μ and 311 μ lines each oscillate in two modes as shown on a recorder trace obtained by mechanically sweeping one of the laser end reflectors. The radiation pattern has been recorded by motor-driving a Golay detector across the output beam. The spatial radiation pattern, which consists of a number of sharp lobes, is extremely sensitive to position of the movable laser cavity end reflector, so much so that in sweeping through a laser line the detector can intercept shifting peaks and valleys of the output pattern. This can give rise to a spurious dip in the laser output mode. Additional wavelength measurements have been made with a two-grooves-per-mm ruled grating mounted in a standard Perkin-Elmer spectrograph. Coherent detection has also been obtained with a millimeter wave crystal diode detector.

P. E. Tannenwald
C. D. Parker
D. F. Nicoli

REFERENCES

1. Solid State Research Report, Lincoln Laboratory, M. I. T. (1966:4), p. 44, DDC 647688.
2. C. R. Whitsett, Phys. Rev. 138, A829 (1965).
3. E. O. Kane, J. Phys. Chem. Solids 1, 249 (1957).
4. J. M. Luttinger, Phys. Rev. 125, 1869 (1962).
5. D. M. Bagguley, M. L. A. Robinson and R. A. Stradling, Phys. Letters 6, 143 (1963).
6. R. L. Aggarwal, Bull. Am. Phys. Soc. 12, 100 (1967).
7. C. R. Pidgeon, S. H. Groves and J. Feinleib, "Electroreflectance Study of Interband Magneto-Optical Transitions in InAs and InSb at 1.5°K," to be published by Solid State Commun.
8. R. N. Brown, J. G. Mavroides and B. Lax, Phys. Rev. 129, 2055 (1963).
9. P. A. Wolff, Phys. Chem. Solids 25, 1057 (1964).
10. B. Lax, K. J. Button, H. J. Zeiger and L. M. Roth, Phys. Rev. 102, 715 (1956).
11. G. A. Baraff, Phys. Rev. 137, A842 (1965).
12. J. Hanus, J. Feinleib and W. J. Scouler, Phys. Rev. Letters 19, 16 (1967).
13. Ref. 1, p. 39.
14. L. L. Van Zandt, J. M. Honig and J. B. Goodenough, Proceedings of the International Conference on Magnetism, Boston, 1967 (to be published).
15. M. H. Cohen, Phys. Rev. 121, 387 (1961).

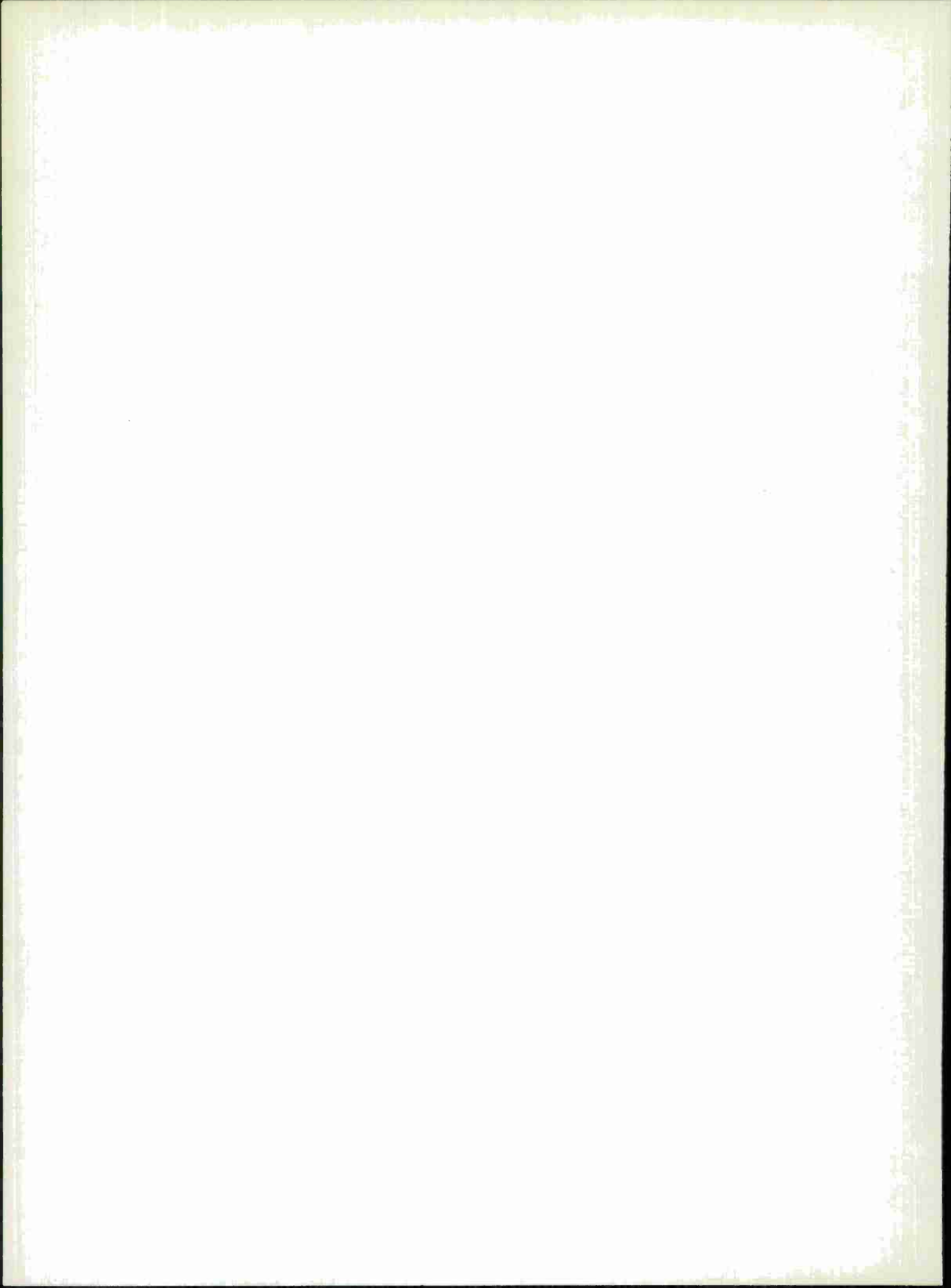
Section IV

16. J.C. Slater, Quantum Theory of Molecules and Solids, Vol. 2 (McGraw-Hill Book Company, Inc., New York, 1965), p.418.
17. E.P. Warekois, J. Appl. Phys. Suppl. 31, 346S (1960).
18. J. Feinleib and W. Paul, Phys. Rev. 155, 841 (1967).
19. J.S. Kouvel and M.E. Fisher, Phys. Rev. 136, A1626 (1964).
20. H.E. Stanley, Phys. Rev. 158, 546 (1967).
21. J.E. Noakes, N.E. Tornberg and A. Arrott, J. Appl. Phys. 37, 1264 (1964).
22. C.D. Graham, Jr., J. Appl. Phys. 36, 1135 (1965); A.R. Miedema, H. Van Kempen and W.J. Huiskamp, Physica 29, 1266 (1963); G. Gorodetsky, S. Shtrikman and D. Treves, Solid State Commun. 4, 147 (1966).
23. R.V. Colvin and S. Araj, J. Phys. Chem. Solids 26, 435 (1965).
24. M.E. Fisher, Critical Phenomena, M.S. Green and J.V. Sengers, Eds. (N.B.S. Miscellaneous Publishers, 273, 1966), p.21.
25. B. Widom and O.K. Rice, J. Chem. Phys. 23, 1250 (1955).
26. M.S. Green, M. Vicenti-Missoni and J.M.H. Levelt Sengers, Phys. Rev. Letters 18, 1113 (1967).
27. A. Mooradian and G.B. Wright, Phys. Rev. Letters 16, 999 (1966).
28. A.L. McWhorter and P.N. Argyres, Bull. Am. Phys. Soc. 12, 102 (1967).
29. R. Loudon, Advan. Phys. 13, 423 (1964).
30. A. Mooradian and A.L. McWhorter (to be published in Phys. Rev. Letters).
31. P.D. Maker and R.W. Terhune, Phys. Rev. 137, A801 (1965).
32. Solid State Research Report, Lincoln Laboratory, M.I.T. (1967:2), p.45, DDC 656548.
33. K. Gustafson, P. DeMartini, C.H. Townes and P.L. Kelley, Bull. APS 12, 687 (1967); F. DeMartini, C.H. Townes, K. Gustafson and P.L. Kelley, Phys. Rev. (to be published); R.J. Joenk and R. Landauer, Phys. Letters 24A, 228 (1967).
34. R. Brewer, Phys. Rev. Letters 19, 8 (1967).
35. H.P.H. Grieneisen and C.A. Sacchi, Bull. APS 12, 686 (1967).

DOCUMENT CONTROL DATA - R&D

(Security classification of title, body of abstract and indexing annotation must be entered when the overall report is classified)

1. ORIGINATING ACTIVITY (Corporate author) Lincoln Laboratory, M.I.T.		2a. REPORT SECURITY CLASSIFICATION Unclassified	
		2b. GROUP None	
3. REPORT TITLE Solid State Research			
4. DESCRIPTIVE NOTES (Type of report and inclusive dates) Quarterly Technical Summary - 1 May through 31 July 1967			
5. AUTHOR(S) (Last name, first name, initial) McWhorter, Alan L.			
6. REPORT DATE 15 August 1967		7a. TOTAL NO. OF PAGES 72	7b. NO. OF REFS 84
8a. CONTRACT OR GRANT NO. AF 19(628)-5167		9a. ORIGINATOR'S REPORT NUMBER(S) Solid State Research (1967:3)	
b. PROJECT NO. 649L		9b. OTHER REPORT NO(S) (Any other numbers that may be assigned this report) ESD-TR-67-467	
c.			
d.			
10. AVAILABILITY/LIMITATION NOTICES This document has been approved for public release and sale; its distribution is unlimited.			
11. SUPPLEMENTARY NOTES None		12. SPONSORING MILITARY ACTIVITY Air Force Systems Command, USAF	
13. ABSTRACT This report covers in detail the solid state research work at Lincoln Laboratory for the period 1 May through 31 July 1967. The topics covered are Solid State Device Research, Optical Techniques and Devices, Materials Research, and Physics of Solids.			
14. KEY WORDS solid state devices electron beam pumping optical techniques and devices laser research materials research band structure Raman scattering magnetoabsorption vapor growth magnetoreflexion Fourier expansion Gunn effect oscillators magnetism Faraday isolator optical heterodyne detection crystal growth electroluminescence magneto-optical research			



Printed by
United States Air Force
L. G. Hanscom Field
Bedford, Massachusetts

